JM PAPERS

Dynamics of turbulence production by attenuating interfacial gravity waves observed in air–water coupled wave-resolving simulation

Yasushi Fujiwara†

Graduate School of Maritime Sciences, Kobe University, Kobe, 6580022, Japan

Even without breaking or wind influence, ocean surface waves are observed to produce turbulence in the water, possibly influencing ocean surface dynamics and air–sea interactions. Based on the water-side free-surface simulations, recent studies suggest that such turbulence is produced through the interaction between the waves and the near-surface Eulerian current associated with the viscous attenuation of waves. To clarify the dynamical role of the air–water interface in the turbulence production, the attenuating interfacial gravity waves were simulated directly using a newly developed two-phase wave-resolving numerical model. The air–water coupling enhanced the wave energy dissipation through the formation of a strong shear at the air-side viscous boundary layer. This led to an enhancement of the wave-to-current momentum transfer and the formation of the down-wave Eulerian mean sheared current, which is favourable for the CL2 instability responsible for the production of Langmuir circulations. As a result, the water-side turbulence grew stronger compared with the corresponding free surface (water-only) wave-resolving simulation. The evolution of the wave-averaged field was well reproduced with the Craik–Leibovich equation with the upper boundary condition provided with the virtual wave stress based on linear theory. The wave energy dissipation by air–water coupling plays a significant role in the quantitative understanding of the wave-induced turbulence at the laboratory and field scales.

Key words: wind–wave interactions, surface gravity waves, air–sea interactions

1. Introduction

Ocean surface waves induce surface turbulent mixing and moderate the exchange of heat, materials and momentum between the atmosphere and the ocean (Sullivan & McWilliams 2010). Waves can produce turbulence even without breaking, a representative process being Langmuir circulations (LCs) (Langmuir 1938). LCs are roll-shaped flow structures

† Email address for correspondence: fujiwara@port.kobe-u.ac.jp

aligned with wave direction, often turbulent, and visualised through the streaks of flotsam accumulated on the convergence zones. They are considered to arise through the instability of a vertically sheared current under the influence of the wave-associated Stokes drift. Its dynamics are described in a wave-averaged framework called the Craik–Leibovich (CL) equation (Craik & Leibovich 1976), and the instability is called the CL2 mechanism (Leibovich 1983). The instability condition requires that the Eulerian current shear $\partial \bar{u}^E / \partial z$ and the Stokes drift shear $\partial u^{St} / \partial z$ have the same sign. Here, $\bar{u}^E$ is wave-averaged Eulerian current, u^{St} is the Stokes drift and z is the vertical coordinate with positive upwards. This sheared Eulerian current is commonly considered to originate from wind stress, which is aligned with the Stokes drift direction in most cases. Belcher *et al.* (2012) estimated the LCs' contributions to the ocean surface mixing based on the CL theory and suggested that the Langmuir mixing plays a major role in many parts of the ocean.

Although the turbulence production by the CL2 mechanism requires the influence of wind, some studies report that waves produce turbulence even without wind, a phenomenon often termed 'non-breaking wave-induced turbulence'. To distinguish from LCs, it is hereinafter called 'windless' (WL) turbulence in this article. Multiple laboratory studies support the presence of WL turbulence, demonstrating turbulence growth under waves generated by a wavemaker (Babanin & Haus 2009; Dai *et al.* 2010; Savelyev, Maxeiner & Chalikov 2012). The mechanism for this phenomenon was originally proposed to be the turbulence transition of the wave orbital motion (Babanin 2006), and parameterisations were developed for large-scale ocean models based on this idea (Pleskachevsky *et al.* 2011). Wu, Rutgersson & Sahlée (2015) estimated the contribution of WL turbulence to the ocean surface mixing based on this parameterisation and concluded that it has a major influence on the total turbulence production. However, the validation of the WL turbulence production mechanism has been limited in both theoretical and experimental aspects, leading to questions raised against the validity of the turbulence transition hypothesis (e.g. D'Asaro 2014). Furthermore, Villas Bôas *et al.* (2019) points out the unclarity in the distinction between WL turbulence and LCs. Clarifying the WL turbulence production mechanism is crucial for developing a parameterisation scheme widely accepted by the modelling community and integrating the two phenomena branches to accurately model wave-induced mixing.

The advancement of numerical modelling and computational resources have enabled us to directly solve the Navier–Stokes equation in free-surface configurations. In such numerical studies, we can strictly control the wind and wave conditions and analyse the three-dimensional structure of turbulence, both of which are difficult in laboratory and field measurements. Tsai *et al.* (2013) studied the water turbulence under wind- and wave-forced conditions and its contribution to gas exchange across the water surface, using the fully nonlinear free surface model described in Tsai & Hung (2007). A similar situation is also studied by Tsai & Lu (2023) with an even more sophisticated analysis of the multiscale vortex structures in the water. Yang & Shen (2011*a*) similarly developed a fully nonlinear free-surface model, and in the accompanying paper (Yang & Shen 2011*b*) they proposed a method to dynamically couple multiple domains to simulate two-phase flow with a deformable interface. Xuan & Shen (2019) proposed an improved scheme for the water-side simulation using flux-form formulation. Guo & Shen (2013, 2014) studied the vorticity kinematics and the turbulence dynamics of turbulence produced by external forcing in the subsurface layer and its interaction with the surface wave motions. Xuan, Deng & Shen (2019) also conducted a detailed dynamical analysis of Langmuir turbulence driven by the surface shear stress and wave motions. Wang & Özgökmen (2018), Fujiwara, Yoshikawa & Matsumura (2018) and Fujiwara & Yoshikawa (2020)

compared the wave-resolving simulation results with the CL equation to study the dynamics of LCs.

Among such studies, Tsai *et al.* (2017) and Fujiwara, Yoshikawa & Matsumura (2020) have provided new insights into the connection between the mechanisms of the WL turbulence and the LCs. These studies suggest that the near-surface shear flow, known as the Eulerian mean drift, plays a central role in turbulence production. Longuet-Higgins (1953) considered the mass transport (Lagrangian) velocity of the waves under an influence of weak viscosity and demonstrated that the vertical shear of the mass transport velocity near the surface would be twice as much as the Stokes drift shear: $\partial(\bar{u}^E + u^{St})/\partial z = 2\partial u^{St}/\partial z$. This Eulerian shear formation is understood through the momentum transfer from the surface waves attenuating due to water viscosity. Consider a small-amplitude, monochromatic deep-water wave with gravitational acceleration g, water density ρ_o, water kinematic viscosity ν_o, amplitude $a(t)$, wavenumber k and angular frequency σ, where the viscous influence is sufficiently small that $\sigma = (gk)^{1/2}$ and $a^{-1}\mathrm{d}a/\mathrm{d}t \ll \sigma$. Lamb (1932) showed that the amplitude attenuation rate $\gamma \equiv -a^{-1}\mathrm{d}a/\mathrm{d}t$ for such a wave would be

$$\gamma_o = 2\nu_o k^2 = \frac{2}{Re_o}\sigma, \tag{1.1}$$

where $Re_o \equiv \sigma k^{-2}/\nu_o$ is the water-side Reynolds number based on wavenumber and wave phase speed. The potential motion of the wave conveys horizontal momentum of $M_o \equiv \rho_o g \sigma a^2/2$ per unit horizontal area. When the waves attenuate following (1.1), $-\mathrm{d}M_o/\mathrm{d}t$ per unit area must be transformed to the Eulerian current. This can be only achieved via the viscous diffusion from the surface boundary layer. Therefore, the following amount of horizontal momentum is received by the Eulerian current (e.g. Phillips 1966):

$$\tau_o^{vws} = \rho_o \nu_o \frac{\partial \bar{u}^E}{\partial z} = 2\gamma_o \times \frac{1}{2}\rho_o \sigma a^2 = \frac{2}{Re_o}\rho_o a^2 \sigma^2. \tag{1.2}$$

This viscous momentum flux was called 'virtual wave stress' by Longuet-Higgins (1969), providing a boundary condition for $\bar{u}^E$ as $\partial \bar{u}^E/\partial z = \partial u^{St}/\partial z$.

The importance of the Eulerian mean drift was elucidated by the wave-resolving direct numerical simulations (DNS). Tsai, Chen & Lu (2015); Tsai *et al.* (2017) and Fujiwara *et al.* (2020) used free-surface models that explicitly solve the deformable surface motion under the fully nonlinear boundary conditions, considering that the surface does not overturn. They all reproduced elongated streamwise vortices as was observed in the tank experiment by Savelyev *et al.* (2012). First, Tsai *et al.* (2015) conducted a simulation of propagating surface waves over a turbulence field and observed a significant growth of initial turbulence. The resulting flow field showed vortical structures with a growth rate consistent with the model of Teixeira & Belcher (2002) based on the rapid distortion theory. Tsai *et al.* (2017) further investigated the streamwise vortices with an increased number of simulations and compared their structure with the linear stability analysis of the CL equation. When the Eulerian current shear is provided by the theory of Longuet-Higgins (1953), the theoretically predicted spanwise wavenumber of the fastest growth mode was close to that of the simulated streamwise vortices. Then, Fujiwara *et al.* (2020) compared a low-Reynolds number wave-resolving DNS and its wave-averaged counterpart using the CL equation with and without virtual wave stress effect. As a result, the temporal evolution of vertical circulation in wave-resolving DNS was very well-reproduced with the CL equation using the virtual wave stress effect. The results of Tsai *et al.* (2017) and Fujiwara *et al.* (2020) suggested that the simulated WL turbulence was driven by the CL2 mechanism associated with the virtual wave stress-driven

sheared current. The latest numerical study by Imamura, Yoshikawa & Fujiwara (n.d.) observed that such vortical flows actually induce turbulent mixing. Through a detailed enstrophy budget analysis, they demonstrated that the turbulence was not locally produced from the orbital motion but non-locally through the sheared current near the surface.

These studies considered the problem in the water-side-only framework, but the water surface is in contact with air in reality. In the water-side-only problem, the viscous energy dissipation occurs over the bulk of water volume (Phillips 1966), and the momentum lost from the wave is received by the vortical current of water. In the presence of the air above, the two fluids can exchange momentum and energy, which can make a difference in the resulting flow fields. Thus, it is important to understand the roles played by the air–water coupling in the attenuating interfacial gravity waves and associated wave-induced turbulence. For this purpose, the wave-resolving numerical simulation is a promising approach because it enables us to evaluate the dynamical interaction between the two phases in detail, which is extremely difficult in laboratory and field measurements. Because the exchange of momentum and energy between water and air is central in this phenomenon, the simulations need to be conducted in air–water coupled configurations, rather than air-side only simulations (e.g. Sullivan, McWilliams & Moeng 2000; Sullivan *et al.* 2008; Cao & Shen 2021), where the water surface serves as the infinite reservoir of energy.

The numerical study of air–water two-phase flow has a long history, with diverse topics of interest and numerical techniques to represent this complex system. For example, the main interest of studies using the interface-following coordinate (as in the present study) includes wind wave generation (Fulgosi *et al.* 2003; Lin *et al.* 2008; Zonta, Soldati & Onorato 2015; Li & Shen 2022), transient adjustment of waves to wind in high-wave-age (Zonta, Onorato & Soldati 2016), and the wind turbulence over waves and the evolution of wave spectrum under wind influence (Hao & Shen 2019). Nevertheless, wind is present in all of these simulations, which makes it difficult to separately discuss the role of air–water coupling in WL turbulence production.

One important theoretical prediction is that the Eulerian mean current is intensified in the presence of air if its mean horizontal motion (mean wind) is zero. Dore (1978) studied the linear theory of interfacial gravity waves under the influence of weak viscosity in both air and water. The horizontal orbital velocity of the irrotational waves is discontinuous at the interface, so the viscous boundary layer (Stokes layer) develops on both sides to match the air- and water-side velocity. Due to the large density ratio, a very sharp shear layer arises in the air side, where a strong energy dissipation occurs. As a result, the leading-order amplitude decay rate is expressed as the sum of the dissipation in the bulk of the water and in the Stokes layer of the air. The result of Dore (1978) can be rewritten for deep-water interfacial waves as follows:

$$\gamma_{ao} = 2\nu_o k^2 + \frac{\rho_a}{\rho_o}(2\nu_a k^2 \sigma)^{1/2} = \left[\frac{2}{Re_o} + \frac{\rho_a}{\rho_o}\left(\frac{2}{Re_a}\right)^{1/2} \right] \sigma, \qquad (1.3)$$

where ρ_a is the density of air, ν_a is the kinematic viscosity of air and $Re_a \equiv \sigma k^{-2}/\nu_a$ is the air-side Reynolds number based on wavenumber and wave phase speed. The relative importance of the two terms depends on scale. Based on physical parameters at $10\,°C$, $\nu_a = 1.4 \times 10^{-5}\,\mathrm{m^2\,s^{-1}}$, $\nu_o = 1.3 \times 10^{-6}\,\mathrm{m^2\,s^{-1}}$, $\rho_a = 1.2\,\mathrm{kg\,m^{-3}}$, and $\rho_o = 1.0 \times 10^3\,\mathrm{kg\,m^{-3}}$ for reference, and using the free surface dispersion relation $\sigma = (gk)^{1/2}$, the ratio of the second to the first term is 0.46, 2.56 and 14.4 for wavelengths of $\lambda = 0.3, 3, 30\,\mathrm{m}$, respectively. For waves longer than $\lambda \approx 0.9\,\mathrm{m}$, the effect of viscous

dissipation in the air dominates over the dissipation in the water. Dore (1978) further investigated the second-order stress at just outside the viscous boundary layer; the results are consistent with the following Eulerian form:

$$\rho_o \nu_o \frac{\partial \bar{u}^E}{\partial z} - \rho_a \nu_a \frac{\partial \bar{u}^E}{\partial z} = \tau_{ao}^{vws} = 2\gamma_{ao} \times \frac{1}{2}\rho_o \sigma a^2 = \left[\frac{2}{Re_o}\rho_o + \left(\frac{2}{Re_a} \right)^{1/2} \rho_a \right] a^2 \sigma^2.$$

(1.4)

Since $\rho_o \nu_o \gg \rho_a \nu_a$, the virtual wave stress is mostly received by the water side term on the left-hand side. Therefore, the theory predicts that the wave momentum is transferred to water with a rate higher than that of the water-only case, possibly leading to stronger WL turbulence production than the free surface simulations.

In this study, the viscous attenuation of air–water interfacial gravity waves and associated WL turbulence production were investigated using two-phase wave-resolving DNS. We aimed to elucidate the effect of air–water coupling on the Eulerian mean current and WL turbulence generation by comparing wave-resolving simulations with and without coupling. Here, the mean airflow is assumed to be zero to clarify the comparison against the water-only simulation, because the wind–wave interaction (e.g. Miles 1957) would complicate the process. However, the knowledge about the boundary layer structure and its role in air–water coupling should still be valid even in the presence of the mean wind. We also investigated the reproducibility of the phenomena in the wave-averaged framework using the wave-averaged simulations incorporating virtual wave stress as the boundary condition. We first extend the wave-resolving numerical model developed by Fujiwara *et al.* (2020) to the two-phase configuration. Its numerical procedure is described in § 2. Then the problem setting for the simulation of attenuating interfacial waves are introduced in § 3, and its results are presented in § 4. Finally, a discussion and conclusions are provided in § 5.

2. Problem settings and numerical scheme

2.1. *Framework*

Here, we describe the numerical scheme of the two-phase flow solver. Various approaches have been used to simulate the air–water interface problems, such as the marker-and-cell method (Harlow & Welch 1965), the volume-of-fluid method (Popinet 2003), the level-set method (Sussman *et al.* 1999), the smoothed particle hydrodynamics (Colagrossi & Landrini 2003), the direct method using the surface-following coordinate and interface tracking (Komori *et al.* 2010; Yang & Shen 2011*b*) and modified or hybrid versions of these algorithms. In the present problem of non-breaking waves, we employ the surface-following coordinate approach, which can retain the sharpness of the interface and easily cluster the grid points to resolve the thin boundary layer. This approach also has an advantage in the conservation of mass, momentum and energy with a moderate computational cost, if a proper numerical method is employed. Here we assume that the air–water interface would not turn over and the interface can be represented with a one-valued function of horizontal position and time. This assumption allows us to prescribe a simple mapping from the physical to the computational domain (vertical coordinate transformation) and to avoid the regridding in each time step. Such a strategy has been adopted for simulating free-surface water-side flows (Tsai & Hung 2007; Yang & Shen 2011*a*; Xuan & Shen 2019), the air-side flows (Sullivan *et al.* 2000, 2008) and the air–water coupled flows (Yang & Shen 2011*b*). The numerical scheme is formulated

as an extension of the framework of the free-surface (water-side) model of Fujiwara *et al.* (2020).

Consider a three-dimensional rectangular domain, where the horizontal boundaries are doubly periodic, and the top and bottom boundaries are rigid walls. The Cartesian coordinates are denoted by x, y (horizontal) and z (vertical). The top and bottom boundaries are denoted by $z = H_a$ and $z = -H_o$, respectively. Here, for simplicity, we assume that the top and bottom walls are flat, but the numerical method described in the following can be easily extended to spatially varying H_a and H_o.

The domain is filled with two incompressible fluids with different densities, which are hereinafter called 'air' and 'water'. The densities of each fluid are ρ_a (air) and ρ_o (water), and $\rho_a < \rho_o$. Here $z = 0$ is taken as the interface location at the state of rest, so the mean vertical thickness of each phase is H_a (air) and H_o (water). The air and water occupy the region $\eta(x, y, t) \le z \le H_a$ and $-H_o \le z \le \eta(x, y, t)$, respectively, where η is assumed to be a one-valued function of x, y and t (time). With this assumption, we disregard the situation where the interfacial overturn (plunging breaker) occurs.

The fluids follow the incompressible Navier–Stokes equation:

$$\frac{\partial u}{\partial t} + u\frac{\partial u}{\partial x} + v\frac{\partial u}{\partial y} + w\frac{\partial u}{\partial z} = -\frac{\partial}{\partial x}(g\eta + p_{nh}) + \frac{\partial T^{xx}}{\partial x} + \frac{\partial T^{yx}}{\partial y} + \frac{\partial T^{zx}}{\partial z}, \quad (2.1a)$$

$$\frac{\partial v}{\partial t} + u\frac{\partial v}{\partial x} + v\frac{\partial v}{\partial y} + w\frac{\partial v}{\partial z} = -\frac{\partial}{\partial y}(g\eta + p_{nh}) + \frac{\partial T^{xy}}{\partial x} + \frac{\partial T^{yy}}{\partial y} + \frac{\partial T^{zy}}{\partial z}, \quad (2.1b)$$

$$\frac{\partial w}{\partial t} + u\frac{\partial w}{\partial x} + v\frac{\partial w}{\partial y} + w\frac{\partial w}{\partial z} = -\frac{\partial p_{nh}}{\partial z} + \frac{\partial T^{xz}}{\partial x} + \frac{\partial T^{yz}}{\partial y} + \frac{\partial T^{zz}}{\partial z}, \quad (2.1c)$$

$$\frac{\partial u}{\partial x} + \frac{\partial v}{\partial y} + \frac{\partial w}{\partial z} = 0. \quad (2.1d)$$

Here, u, v and w are x-, y-, and z-component velocities, respectively, T^{xx} and so on are the components of kinematic viscous stress tensor $\boldsymbol{T}$ (i.e. viscous stress tensor divided by density) and g is gravitational acceleration. In (2.1), the total pressure $\tilde{p}$ is decomposed into the hydrostatic and non-hydrostatic components, $\tilde{p} = \rho g(\eta - z) + \tilde{p}_{nh} = \rho g(\eta - z) + \rho p_{nh}$, where $\tilde{p}_{nh} \equiv \rho p_{nh}$ and ρ is the density (ρ_a or ρ_o). The viscous stress can be written as

$$T^{x_i x_j} = \nu\left(\frac{\partial u_i}{\partial x_j} + \frac{\partial u_j}{\partial x_i}\right), \quad (2.2)$$

where $i, j = 1, 2, 3$, $(x_1, x_2, x_3) = (x, y, z)$ and $(u_1, u_2, u_3) = (u, v, w)$. The kinematic viscosity ν can be either constant or some eddy viscosity modelled with the velocity field.

At the top and bottom ($z = H_a, -H_o$), $w = 0$ is demanded as the kinematic boundary condition. When $\nu \ne 0$, dynamic boundary conditions must be provided there, such as the no-slip condition ($(u, v, w)_{air} = (u, v, w)_{water}$) or some momentum flux parameterisation ($\rho T^{xz} = \tau^x$, $\rho T^{yz} = \tau^y$). At the interface $z = \eta(x, y, t)$, the mass continuity is demanded as the kinematic boundary condition:

$$\frac{\partial \eta}{\partial t} = w - u\frac{\partial \eta}{\partial x} - v\frac{\partial \eta}{\partial y}, \quad \text{at } z = \eta + 0, \eta - 0. \quad (2.3)$$

Here, this condition is satisfied at both the air ($z = \eta + 0$) and water ($z = \eta - 0$) sides. By vertically integrating the continuity equation (2.1d) from the top or bottom to the interface

999 A97-6

and using this condition, one obtains the column mass conservation equation:

$$\frac{\partial \eta}{\partial t} = \frac{\partial}{\partial x} \int_{\eta}^{H_a} u \, dz + \frac{\partial}{\partial y} \int_{\eta}^{H_a} v \, dz, \qquad (2.4a)$$

$$\frac{\partial \eta}{\partial t} = -\frac{\partial}{\partial x} \int_{-H_o}^{\eta} u \, dz - \frac{\partial}{\partial y} \int_{-H_o}^{\eta} v \, dz. \qquad (2.4b)$$

As the dynamic boundary conditions, the continuity of interfacial stress $(-\tilde{p}\boldsymbol{I} + \rho \boldsymbol{T}) \cdot \boldsymbol{n}$ is demanded. Here, $\boldsymbol{n} = (1 + \eta_x^2 + \eta_y^2)^{-1/2}(-\eta_x, -\eta_y, 1)$, denotes the upwards-looking unit normal vector at the interface, where $\eta_x \equiv \partial \eta / \partial x$ and $\eta_y \equiv \partial \eta / \partial y$, and $\boldsymbol{I}$ denotes the unit tensor. We formulated the stress continuity via τ_i^{tx}, τ_i^{ty}, and $-\tilde{p}_{nh} + \tau_i^n$ (subscript i denotes 'interface' and not the coordinate index) in the following equations:

$$\tau_i^{tx} \equiv \rho \boldsymbol{t}^x \cdot \boldsymbol{T} \cdot \boldsymbol{n} = \rho \frac{(1 - \eta_x^2) T^{zx} - \eta_x \eta_y T^{zy} + \eta_x (T^{zz} - T^{xx}) - \eta_y T^{xy}}{\left[(1 + \eta_x^2 + \eta_y^2)(1 + \eta_x^2) \right]^{1/2}}, \qquad (2.5a)$$

$$\tau_i^{ty} \equiv \rho \boldsymbol{t}^y \cdot \boldsymbol{T} \cdot \boldsymbol{n} = \rho \frac{-\eta_x \eta_y T^{zx} + (1 - \eta_y^2) T^{zy} - \eta_x T^{xy} + \eta_y (T^{zz} - T^{yy})}{\left[(1 + \eta_x^2 + \eta_y^2)(1 + \eta_y^2) \right]^{1/2}}, \qquad (2.5b)$$

$$-\tilde{p}_{nh} + \tau_i^n \equiv \boldsymbol{n} \cdot (-\tilde{p}\boldsymbol{I} + \rho \boldsymbol{T}) \cdot \boldsymbol{n}. \qquad (2.5c)$$

Here, $\boldsymbol{t}^x \equiv (1 + \eta_x^2)^{-1/2}(1, 0, \eta_x)$ and $\boldsymbol{t}^y \equiv (1 + \eta_y^2)^{-1/2}(0, 1, \eta_y)$ represent the unit vectors tangential to the interface that lie in x–z and y–z planes, respectively. The tangential stress components τ_i^{tx} and τ_i^{ty} need to be modelled from the neighbouring velocity field, such as the no-slip boundary condition or the bulk formula. Once these are obtained, the normal viscous stress component $\tau_i^n \equiv \rho (1 + \eta_x^2 + \eta_y^2)^{-1}(T^{zz} - 2\eta_x T^{xz} - 2\eta_y T^{yz} + \eta_x^2 T^{xx} + 2\eta_x \eta_y T^{xy} + \eta_y^2 T^{yy})$ was computed explicitly at each side of the interface. To simplify the continuity condition of the non-hydrostatic pressure $(\tilde{p}_{nh} - \tau_i^n)_{air} = (\tilde{p}_{nh} - \tau_i^n)_{water}$, we introduced the pseudo-pressure variable $p \equiv \rho^{-1}[\tilde{p}_{nh}(x, y, z) - \tau_i^n(x, y)]$ and transformed the pressure gradient terms in (2.1) as follows:

$$-\frac{\partial p_{nh}}{\partial x} = -\frac{\partial}{\partial x}\left(p + \frac{\tau_i^n}{\rho} \right), \quad -\frac{\partial p_{nh}}{\partial y} = -\frac{\partial}{\partial y}\left(p + \frac{\tau_i^n}{\rho} \right), \quad -\frac{\partial p_{nh}}{\partial z} = -\frac{\partial p}{\partial z}. \quad (2.6)$$

The pseudo-pressure p multiplied with density is continuous at the interface: $(\rho p)_{air} = (\rho p)_{water}$.

We employed the curvilinear coordinate that follows the interfacial deformation. The independent variables (x, y, z, t) were transformed to (x^*, y^*, z^*, t^*) as

$$x = x^*, \; y = y^*, \; z = z^* + (1 - z^*/H_a)\eta, \; t = t^* \quad \text{(air side)}, \qquad (2.7a)$$

$$x = x^*, \; y = y^*, \; z = z^* + (1 + z^*/H_o)\eta, \; t = t^* \quad \text{(water side)}. \qquad (2.7b)$$

This transformation maps the physical air (water) domain $\eta \leq z \leq H_a$ ($-H_o \leq z \leq \eta$) to the computational domain $0 \leq z^* \leq H_a$ ($-H_o \leq z^* \leq 0$).

After coordinate transformation, the governing equations (2.1) can be written in the following form:

$$\frac{\partial U}{\partial t^*} = -\frac{\partial}{\partial x^*}\left(\frac{UU}{h} + gh\eta + \frac{h\tau_i^n}{\rho} + P - hT^{xx}\right) - \frac{\partial}{\partial y^*}\left(\frac{VU}{h} - hT^{yx}\right)$$
$$- \frac{\partial}{\partial z^*}\left(\frac{\Omega U}{h} - gz_{x^*}\eta - \frac{z_{x^*}\tau_i^n}{\rho} - \frac{z_{x^*}P}{h} + z_{x^*}T^{xx} + z_{y^*}T^{yx} - T^{zx}\right), \quad (2.8a)$$

$$\frac{\partial V}{\partial t^*} = -\frac{\partial}{\partial x^*}\left(\frac{UV}{h} - hT^{xy}\right) - \frac{\partial}{\partial y^*}\left(\frac{VV}{h} + gh\eta + \frac{h\tau_i^n}{\rho} + P - hT^{yy}\right)$$
$$- \frac{\partial}{\partial z^*}\left(\frac{\Omega V}{h} - gz_{y^*}\eta - \frac{z_{y^*}\tau_i^n}{\rho} - \frac{z_{y^*}P}{h} + z_{x^*}T^{xy} + z_{y^*}T^{yy} - T^{zy}\right), \quad (2.8b)$$

$$\frac{\partial W}{\partial t^*} = -\frac{\partial}{\partial x^*}\left(\frac{UW}{h} - hT^{xz}\right) - \frac{\partial}{\partial y^*}\left(\frac{VW}{h} - hT^{yz}\right)$$
$$- \frac{\partial}{\partial z^*}\left(\frac{\Omega W}{h} + \frac{P}{h} + z_{x^*}T^{xz} + z_{y^*}T^{yz} - T^{zz}\right), \quad (2.8c)$$

$$\frac{\partial U}{\partial x^*} + \frac{\partial V}{\partial y^*} + \frac{\partial}{\partial z^*}\left(\frac{W}{h} - \frac{z_{x^*}U}{h} - \frac{z_{y^*}V}{h}\right) = 0. \quad (2.8d)$$

Here, subscripts t^*, x^*, y^* and z^* denote partial derivatives, $h \equiv \partial z/\partial z^*$ is the layer thickness, $U \equiv hu$, $V \equiv hv$, $W \equiv hw$ and $P \equiv hp$ are the layer thickness-weighted variables and $\Omega \equiv w - z_{t^*} - uz_{x^*} - vz_{y^*}$ is the layer thickness-weighted z^*-velocity. The apparent form of (2.8) is identical for both air and water. However, the expressions for h and other variables vary because the definition of z (2.7) depends on the fluid type. The column-mass conservation equation (2.4) can be transformed as follows:

$$\frac{\partial \eta}{\partial t^*} = \frac{\partial}{\partial x^*}\int_0^{H_a} U\, dz^* + \frac{\partial}{\partial y^*}\int_0^{H_a} V\, dz^*, \quad (2.9a)$$

$$\frac{\partial \eta}{\partial t^*} = -\frac{\partial}{\partial x^*}\int_{-H_o}^0 U\, dz^* - \frac{\partial}{\partial y^*}\int_{-H_o}^0 V\, dz^*. \quad (2.9b)$$

2.2. *Spatial discretisation*

Taking advantage of the doubly periodic horizontal boundary condition, we discretise the variables in equally spaced grid points in x^* and y^* and take the pseudo-spectral approach to approximate horizontal derivatives. Hereinafter, $\partial/\partial x^*$ and $\partial/\partial y^*$ represent the evaluation of horizontal derivatives using the fast Fourier transform algorithm. To avoid nonlinear instability, spectral coefficients above two-thirds of Nyquist frequency are filled with zeros.

In vertical, the second-order finite-difference method is used. The air-side (water-side) domain $0 \leq z^* \leq H_a$ ($-H_o \leq z^* \leq 0$) is discretised as layers with variable thickness, and variables are placed in a staggered grid layout (figure 1). Horizontal velocity components and scalars are defined at layer centres, and vertical velocity components are defined at layer interfaces. Both air- and water-side W are defined at the air–water interface because the velocity discontinuity may arise there unless the no-slip boundary condition is assumed. The thickness-weighted pseudo-pressure P is defined not only at layer centres but also at the air–water interface. Denoting the numbers of layers with K_a (air) and K_o
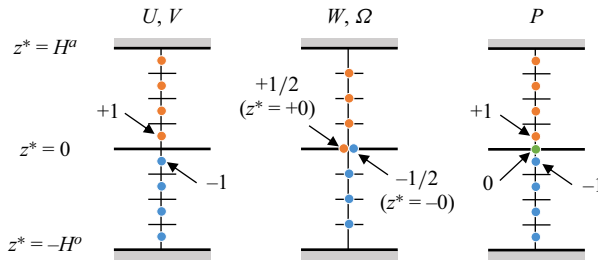
Figure 1. Layout of discretised variables in the vertically staggered grid. Blue, orange and green markers represent the properties of water, air and interface, respectively. Numbers 0, $\pm 1/2$ and ± 1 denote the indices of vertical grid points used in § 2.3.

(water), P is discretised into $K_a + K_o + 1$ points in vertical. This additional degree of freedom allows us to ensure the mass continuity at the interface (2.3), as discussed further in § 2.3. Hereinafter, $\partial/\partial z^*$ represents the second-order finite-difference approximation of vertical derivatives. Horizontal velocity components U and V are defined at the cell centres. When they are required at the air–water interface as in (2.8d), the values at the grid centres just above or below the interface is consistently used to represent the interfacial value. Evaluating (2.9) in the discretised domain and using (2.8d), we obtain

$$\frac{\partial \eta}{\partial t^*} = \sum_k \left(\frac{\partial U_k}{\partial x^*} + \frac{\partial V_k}{\partial y^*} \right) \Delta z_k^* = w_{1/2} - u_1 \eta_x - v_1 \eta_y, \tag{2.10a}$$

$$\frac{\partial \eta}{\partial t^*} = -\sum_k \left(\frac{\partial U_k}{\partial x^*} + \frac{\partial V_k}{\partial y^*} \right) \Delta z_k^* = w_{-1/2} - u_{-1} \eta_x - v_{-1} \eta_y. \tag{2.10b}$$

Here, the subscript k represents vertical coordinate index, where $k = \pm 1$ denote the cell centres next to the interface and $k = \pm 1/2$ denote the variables on each side of the interface (see figure 1). This is the kinematic boundary condition (2.3) represented in the present framework. This approximation contains truncation error of $O(\Delta z^*)$, but it is typically overwhelmed by other discretisation errors (e.g. vertical finite-difference error of $O(\Delta z^{*2})$), as is observed in Appendix A.1.

Note that the continuity of the normal stress is achieved implicitly by introducing the pseudo-pressure at the interface and using the common value for calculating the pressure-gradient force at the air and water side. Similar strategy is adopted to achieve the continuity of the tangential stress: we evaluated τ_i^{tx} and τ_i^{ty} at the interface and used that common value at the air and water side, thereby ensuring the momentum conservation. The method for evaluating the tangential stress is detailed in the following subsection.

2.3. *Temporal integration*

To achieve high accuracy in mass, momentum and energy conservation, the fourth-order Adams–Bashforth (AB4) scheme was adopted for the time integration of velocity field and interface elevation (Fujiwara *et al.* 2020). Hereinafter, we describe the time-advancement method from the known fields of $U^{(n)}$, $V^{(n)}$, $W^{(n)}$ and $\eta^{(n)}$, where superscript (n) denotes the timesteps. Since we employ a fully explicit scheme, all the right-hand side terms of (2.8a–c) and (2.9) are evaluated at timestep n and used for temporal integration. The terms at past three timesteps $(n-1, n-2, n-3)$ are stored for the AB4 scheme, but when

the stability limit of some terms (e.g. viscosity) is much looser than that required by the interfacial waves, lower-order explicit schemes can be used to reduce computational cost without much truncation error.

The viscous stress tensor T^{ij} is diagnostically evaluated from $(U^{(n)}, V^{(n)}, W^{(n)})$. At the air–water interface, the tangential components $(\tau_i^{tx}, \tau_i^{ty})$ are required to be continuous across the interface. They are evaluated referring to the velocity at the bottom layer of the air and the top layer of the water. In the case of the no-slip boundary condition, the velocity at the interface $z^* = 0$ is approximated with the value at $z^* = -0.5\Delta z^*$ (top layer of water) due to the large density ratio. The tangential stress $(\tau_i^{tx}, \tau_i^{ty})$ is evaluated from the velocity difference between the lowest layer of the air and the interface. Then $(\tau_i^{tx}, \tau_i^{ty})$ is used to determine the boundary values of the water-side viscous stress tensor, together with τ_i^n, which is independently evaluated at each side. Due to the approximation of interfacial velocity using the first grid point, the consistency between the tangential stress and the surrounding velocity is not strictly satisfied. However, the relative error induced by this approximation (difference between 'true' interfacial velocity and the top layer of water) would be small as discussed in the following. The error can be roughly estimated from the leading-order stress balance $\rho_a v_a (\mathrm{d}u/\mathrm{d}z)_a = \rho_o v_o (\mathrm{d}u/\mathrm{d}z)_o$. The difference between the true interfacial velocity u_i and approximated velocity is estimated by

$$u(-0.5\Delta z^*) - u_i = 0.5\Delta z^* \left(\frac{\mathrm{d}u}{\mathrm{d}z}\right)_o \approx 0.5\Delta z^* \frac{\rho_a v_a}{\rho_o v_o}\left(\frac{\mathrm{d}u}{\mathrm{d}z}\right)_a \approx \frac{\rho_a v_a}{\rho_o v_o}(u(0.5\Delta z^*) - u_i),$$

(2.11)

where the grid thicknesses at the air and water sides are assumed similar. Therefore, the relative error is estimated as $O(\rho_a v_a/\rho_o v_o)$, which is typically of $O(10^{-2})$, assuming $\rho_a v_a/\rho_o v_o \ll 1$ and $u(-0.5\Delta z^*) \sim u(0.5\Delta z^*)$. Furthermore, as long as the tangential stress imposed for each phase is identical, local momentum conservation is satisfied. Therefore, the present approximation saves us from an iterative approach for velocity–stress consistency without much disadvantage in accuracy. The error caused by this approximation is evaluated in Appendix C.

In the present model with variable vertical layer thickness, the temporal integration of the viscosity term using an explicit scheme would impose a severe limitation on the time step for a stable computation. However, the CFL condition regarding the interfacial gravity wave mode, which need to solve accurately, is similarly strict, even with the vertical resolution high enough to resolve the Stokes boundary layer (SBL) with several layers. Therefore, we employ the explicit scheme for the integration of viscous terms and do not employ the implicit scheme that requires iteration.

To integrate the pressure gradient terms in (2.8) using the AB4 scheme, the instantaneous pressure field $P^{(n)}$ is needed. The pressure field must satisfy the normal stress continuity equation (2.5c) and retain the velocity incompressibility. Such pressure field must be obtained through a Poisson equation with non-constant coefficients that require an iterative approach to solve. In some preceding air–water coupled numerical models, the air–water coupling was achieved by alternatively solving for each phase, where the single-phase solution is used as the boundary condition for the other phase (see the detailed discussion given in, e.g. Lombardi, De Angelis & Banerjee 1996; Yang & Shen 2011b). In the present model, we derive the pressure field based on the air–water coupled pressure Poisson equation, which is solved in a single-loop iteration, since the numerical accuracy of the pressure field matters in the problems of our concern.

To obtain the instantaneous pressure field, we constructed a pressure Poisson equation for $P^{(n)}$ as follows. The time derivative of incompressibility relation (2.8d) is

$$
\frac{\partial U_{t^*}}{\partial x^*} + \frac{\partial V_{t^*}}{\partial y^*} + \frac{\partial}{\partial z^*} \left(\frac{W_{t^*}}{h} - \frac{z_{x^*} U_{t^*}}{h} - \frac{z_{y^*} V_{t^*}}{h} \right)
$$
$$
+ \frac{\partial}{\partial z^*} \left[\left(\frac{1}{h} \right)_{t^*} W - \left(\frac{z_{x^*}}{h} \right)_{t^*} U - \left(\frac{z_{y^*}}{h} \right)_{t^*} V \right] = 0. \tag{2.12}
$$

By substituting (2.8a–c), we obtain

$$
\left(\frac{\partial^2}{\partial x^{*2}} + \frac{\partial^2}{\partial y^{*2}} + \frac{\partial^2}{\partial z^{*2}} \right) P = \left(1 - \frac{1}{h^2} \right) \frac{\partial^2 P}{\partial z^{*2}}
$$
$$
+ \frac{1}{h^2} \frac{\partial}{\partial z^*} \left[h(z_{x^*} P)_{x^*} + h(z_{y^*} P)_{y^*} + h z_{x^*} P_{x^*} + h z_{y^*} P_{y^*} - z_{x^*} (z_{x^*} P)_{z^*} - z_{y^*} (z_{y^*} P)_{z^*} \right]
$$
$$
+ \frac{\partial G^x}{\partial x^*} + \frac{\partial G^y}{\partial y^*} + \frac{1}{h} \frac{\partial}{\partial z^*} (G^z - z_{x^*} G^x - z_{y^*} G^y) + \frac{\partial}{\partial z^*} \left[\left(\frac{1}{h} \right)_{t^*} W - \left(\frac{z_{x^*}}{h} \right)_{t^*} U - \left(\frac{z_{y^*}}{h} \right)_{t^*} V \right], \tag{2.13}
$$

where G^x, G^y and G^z denote the right-hand-side terms in (2.8a–c) that can be evaluated explicitly, i.e. terms that do not include P, and the timestep index (n) is omitted. We separated the constant-coefficient terms in the Laplacian of P into the left-hand side, and the time derivatives of the metric variables h and z were explicitly evaluated using (2.9). This relation holds for each discretised layer, so the number of equations per vertical column was $K_a + K_o$. One more equation per column was needed to obtain P, which has $K_a + K_o + 1$ degrees of freedom in vertical. For this, we employed the mass continuity equation at the interface (2.3). Equating the right-hand sides of (2.10) and taking a time derivative, we obtained

$$
\frac{1}{h_a} \left(\frac{\partial W}{\partial t^*} \right)_{1/2} - \frac{\eta_{x^*}}{h_a} \left(\frac{\partial U}{\partial t^*} \right)_1 - \frac{\eta_{y^*}}{h_a} \left(\frac{\partial V}{\partial t^*} \right)_1 + \left(\frac{1}{h_a} \right)_{t^*} W_{1/2} - \left(\frac{\eta_{x^*}}{h_a} \right)_{t^*} U_1 - \left(\frac{\eta_{y^*}}{h_a} \right)_{t^*} V_1
$$
$$
= \frac{1}{h_o} \left(\frac{\partial W}{\partial t^*} \right)_{-1/2} - \frac{\eta_{x^*}}{h_o} \left(\frac{\partial U}{\partial t^*} \right)_{-1} - \frac{\eta_{y^*}}{h_o} \left(\frac{\partial V}{\partial t^*} \right)_{-1} + \left(\frac{1}{h_o} \right)_{t^*} W_{-1/2} - \left(\frac{\eta_{x^*}}{h_o} \right)_{t^*} U_{-1} - \left(\frac{\eta_{y^*}}{h_o} \right)_{t^*} V_{-1}. \tag{2.14}
$$

Variables with subscripts 1 and -1 were evaluated at the layer centres next to the interface in the air and water side, respectively (see figure 1). Similarly, subscripts $1/2$ and $-1/2$ denote the variables on the air and water side, respectively, of the interface $z^* = 0$. By substituting (2.8a–c) to (2.14), we obtained the following equation for P:

$$
\left(-\frac{1}{h_a^2} \frac{\partial P}{\partial z^*} + \frac{G^z}{h_a} \right)_{1/2} - \frac{\eta_{x^*}}{h_a} \left[-\frac{\partial P}{\partial x^*} + \left(\frac{z_{x^*} P}{h_a} \right)_{z^*} + G^x \right]_1 - \frac{\eta_{y^*}}{h_a} \left[-\frac{\partial P}{\partial y^*} + \left(\frac{z_{y^*} P}{h_a} \right)_{z^*} + G^y \right]_1
$$
$$
+ \left(\frac{1}{h_a} \right)_{t^*} W_{1/2} - \left(\frac{\eta_{x^*}}{h_a} \right)_{t^*} U_1 - \left(\frac{\eta_{y^*}}{h_a} \right)_{t^*} V_1
$$
$$
= \left(-\frac{1}{h_o^2} \frac{\partial P}{\partial z^*} + \frac{G^z}{h_o} \right)_{-1/2} - \frac{\eta_{x^*}}{h_o} \left[-\frac{\partial P}{\partial x^*} + \left(\frac{z_{x^*} P}{h_o} \right)_{z^*} + G^x \right]_{-1} - \frac{\eta_{y^*}}{h_o} \left[-\frac{\partial P}{\partial y^*} + \left(\frac{z_{y^*} P}{h_o} \right)_{z^*} + G^y \right]_{-1}
$$
$$
+ \left(\frac{1}{h_o} \right)_{t^*} W_{-1/2} - \left(\frac{\eta_{x^*}}{h_o} \right)_{t^*} U_{-1} - \left(\frac{\eta_{y^*}}{h_o} \right)_{t^*} V_{-1}. \tag{2.15}
$$

The pressure variable notation in this equation requires clarification. From the definition, $P \equiv h_a p$ and $P \equiv h_o p$ in the air side (positive indices) and water side (negative

indices), respectively. Since ρp is continuous at the interface, we introduced $P_0 \equiv \rho p / \sqrt{\rho_a \rho_o}$ for numerical implementation. With these definitions of discretised P, the z^*-derivatives of P in (2.15) should be read as

$$\left(\frac{\partial P}{\partial z^*}\right)_{1/2} = \frac{h_a p_1 - h_a p_0}{\Delta z_1^*/2} = \frac{1}{\Delta z_1^*/2}\left(P_1 - h_a \sqrt{\frac{\rho_o}{\rho_a}} P_0\right), \qquad (2.16)$$

and so on. Similarly, this definition of P_0 was used when evaluating (2.13) at the layers directly above and below the interface.

For each vertical column, (2.13) and (2.15) provided $(K_a + K_o + 1)$ equations with $(K_a + K_o + 1)$ unknown variables $P_{-K_o,\dots,0,\dots,K_a}$. This system was solved by the fixed-point iteration method as described in Sullivan *et al.* (2000) and Fujiwara *et al.* (2020). When the vertical index is denoted with k, (2.13) and (2.15) can be written as

$$\left(\frac{\partial^2}{\partial x^{*2}} + \frac{\partial^2}{\partial y^{*2}}\right)P_k + \left(\frac{\partial^2 P}{\partial z^{*2}}\right)_k = \epsilon(P_{k-1}, P_k, P_{k+1}) + Q_k \quad (k \neq 0), \qquad (2.17a)$$

$$\left(\frac{\partial^2 P}{\partial z^{*2}}\right)_k = \epsilon(P_{k-1}, P_k, P_{k+1}) + Q_k \quad (k = 0). \qquad (2.17b)$$

Here, ϵ is the linear term of P whose coefficients vary in space, and Q represents the terms that do not include P. Denoting the left-hand side terms with $\mathcal{L}(P)$ and the iteration index with superscript [m], we iteratively solved for $P^{[m]}$ in the following equation:

$$\mathcal{L}(P_{k-1}^{[m]}, P_k^{[m]}, P_{k+1}^{[m]}) = \epsilon(P_{k-1}^{[m-1]}, P_k^{[m-1]}, P_{k+1}^{[m-1]}) + Q_k. \qquad (2.18)$$

The inversion of the left-hand side can be achieved by using horizontal fast Fourier transform and tridiagonal solver. Since both the top and bottom boundaries are rigid-lid, one can add an arbitrary constant to the pressure field. We constrained this degree of freedom by demanding that the horizontal average of P_0 is zero. This equation was iteratively solved until all of the normalised residuals

$$\frac{\max|P_{1,\dots,K_a}^{[m]} - P_{1,\dots,K_a}^{[m-1]}|}{\text{r.m.s.}(P_{1,\dots,K_a}^{[m]})}, \frac{\max|P_0^{[m]} - P_0^{[m-1]}|}{\text{r.m.s.}(P_0^{[m]})}, \frac{\max|P_{-K_o,\dots,-1}^{[m]} - P_{-K_o,\dots,-1}^{[m-1]}|}{\text{r.m.s.}(P_{-K_o,\dots,-1}^{[m]})} \qquad (2.19)$$

become smaller than a certain value (typically 10^{-8}), where r.m.s. denotes root mean square over all grid points. This way, the instantaneous pressure field is accurately solved without nested iteration. For the AW-ctrl case introduced in § 3, which is a typical problem with wave slope $ak = 0.1$, the number of iteration required for convergence was seven.

Once the pressure field was obtained, the prognostic equations (2.8a–c) and (2.9b) were integrated with the AB4 scheme. Due to the nonlinearity of the incompressibility equation, the velocity field after the time integration contains a small compressibility of $O(\Delta t^5)$. To fix this, the gradient of a scalar potential was added to the velocity field as in Fujiwara *et al.* (2020). The Poisson equation for the potential was obtained by demanding the incompressibility of the final velocity field. The procedure is very similar to the pressure equations (2.13) and (2.15), so it is not detailed here.

The performance of the numerical model was examined in several benchmark cases, and its results are described in Appendix A. The model well-reproduced the analytic behaviours of interfacial gravity waves and the Miles instability problem with a reasonable spatial resolution. Notably, the flux form configuration and the fully coupled

Case name	Domain	Difference from 'ctrl'
AW-ctrl	Air–water	—
W-ctrl	Water only	—
AW-noturb	Air–water	x–z two-dimensional
W-noturb	Water only	x–z two-dimensional
AW-CL	Air–water	CL equation, described in detail in § 4.4
W-CL	Water only	CL equation, described in detail in § 4.4
AW-deepnoise	Air–water	Initial u noise added to all grid points
AW-a2	Air–water	Initial $a = 0.2$
AW-narrow	Air–water	$L_y = 1.8\pi$
AW-long	Air–water	$L_x = 4\pi, L_y = 1.8\pi$

Table 1. List of cases considered in this study.

pressure-solving strategy led to small numerical errors in the energy, momentum and mass conservation, as demonstrated in § 3. This feature is favourable in considering a delicate problem such as the WL turbulence production.

The numerical procedure can be extended easily to the air-side-only configuration where $\eta(x, y, t)$ is externally provided. Although such a problem is not considered in this article, the numerical procedure is briefly introduced in Appendix B for future reference.

3. Problem set-up

Numerical simulations of attenuating interfacial waves are conducted to clarify the difference in wave-induced turbulence between the air–water coupled flow and the free-surface flow. We consider both the air–water coupled (simulated with the model developed in this study, labelled 'AW') and the water-only (simulated with the free surface model of Fujiwara *et al.* (2020), labelled 'W') configurations. In each configuration, a basic three-dimensional set-up labelled 'ctrl' is considered, and several variants are also designed to study the dynamical roles of particular processes and sensitivity to problem set-up. In table 1, all the set-ups are listed.

We first introduce the air–water coupled configuration. The following description pertains to the AW-ctrl case, whereas the AW-noturb case is derived by assuming homogeneity in the y direction ($\partial/\partial y = 0$). Consider a wavelength λ and non-dimensionalise all the variables based on the spatial scale of $k^{-1} = \lambda/2\pi$ and the temporal scale of $\sigma^{-1} = [gk(\rho_o - \rho_a)/(\rho_o + \rho_a)]^{-1/2}$ (angular frequency of the small-amplitude deep-water wave). For density, the air-side density is used as the reference. Hereinafter, all the symbols denote non-dimensionalised variables. Under this non-dimensionalised system, a three-dimensional domain of $(L_x, L_y, H_a, H_o) = (2\pi, 2.4\pi, 1.5\pi, 1.5\pi)$ was considered. The mean depths of air and water layers are 75 % of a wavelength, which is still in a deep-water regime. Therefore, the wave period is roughly 2π, with small modifications by nonlinearity and finite-depth effects.

This system is characterised by three non-dimensional numbers, namely, the density ratio $r \equiv \rho_o/\rho_a$ and the Reynolds numbers $(Re_a, Re_o) = (\sigma k^{-2}/\nu_a, \sigma k^{-2}/\nu_o)$. We choose the density ratio of $r = 1.0 \times 10^3$ and the Reynolds numbers of $(Re_a, Re_o) = (1.5 \times 10^4, 1.5 \times 10^5)$. This parameter set does not precisely correspond to a particular physical condition because we are mainly focused on the dynamical understanding of the phenomena. Nevertheless, the present parameter choice roughly corresponds to the actual

air–water interfacial wave with $\lambda \approx 1.0\,\mathrm{m}$ ($Re_a = 1.4 \times 10^4$, $Re_o = 1.5 \times 10^5$ and $r = 8.1 \times 10^2$ at $10\,^{\circ}\mathrm{C}$). Here we neglect the effect of surface tension to further simplify the dynamics.

The top and bottom boundaries are flat and free-slip. The no-slip boundary condition is imposed at the air–water interface. Then the domain was discretised with 128 and 320 grid points in x and y directions, respectively. Higher spatial resolution is assumed in y direction because the resulting flow shows a finer structure in y. In the vertical, the air and water domains are discretised with 128 and 160 grid points, respectively. The grid points are clustered near the interface, such that the layer thickness directly above and below the interface would be half of the viscous SBL thickness $(2/Re_{a,o})^{1/2}$, which is thicker in the air side. The layer thickness increased exponentially away from the interface, with ratios of 1.0239 and 1.0270 on the air and water side, respectively.

For the water-only case (W-ctrl and W-noturb), we consider a horizontally rectangular domain topped with a free-surface boundary at its upper surface, $z = \eta(x, y, t)$. The upper surface satisfies the kinematic boundary condition $\partial\eta/\partial t = w - u\partial\eta/\partial x - v\partial\eta/\partial y$ and the no-stress boundary condition $(-\tilde{p}\boldsymbol{I} + \rho\boldsymbol{T}) \cdot \boldsymbol{n} = \boldsymbol{0}$. The bottom boundary is the flat wall with the free-slip condition as in the AW cases. Because the dispersion relation of the surface waves differs from the air–water coupled cases, the reference time scale of $\sigma^{-1} = (gk)^{-1/2}$ was used for the non-dimensionalisation instead. Otherwise, the geometric set-up and parameters are identical to the water side of the AW cases.

In both the AW and W configurations, we initialised the flow field with the orbital velocity of the fifth-order Stokes wave (Tsuji & Nagata (1973) for the AW and Fenton (1985) for the W cases) that propagates towards the x direction, with wavelength 2π and initial wave amplitude of $a = 0.1$ (wave slope of 0.1). The asymptotic solution of Tsuji & Nagata (1973) assumes a deep-water limit, so its use as the initial condition can introduce a spurious response with an interfacial displacement of $O(10^{-3})$. The analysis conducted here is insensitive to the spurious waves of this amount. In the AW-ctrl and W-ctrl cases, a Gaussian noise with a standard deviation of 10^{-3} is added to u at water-side grid points near the interface (only in one layer centred at $z^* = -0.0086$ and $\Delta z^* = 0.0020$ thick) to seed the horizontal inhomogeneity. Before adding to the orbital velocity, the noise field is horizontally low-pass filtered at a cutoff wavenumber of 16. Then, the divergent component of the noise field is removed and made solenoidal in the projection procedure during the initialisation of the simulation. We expect that the resulting turbulence is insensitive to this noise structure because of inherent instability (Tsai *et al.* 2017; Fujiwara *et al.* 2020). To examine the dependence of the result on initial noise structure, we have conducted an AW case with the same amplitude noise added to the grid points of all levels in the water side, which is named the 'AW-deepnoise' case. In addition, to study the phenomenon under larger wave amplitude, an AW case with doubled initial wave amplitude (AW-a2) was conducted. We also conducted the sensitivity study to the domain size (AW-long and AW-narrow), which is described in Appendix E.

Starting from this initial velocity field, the temporal integration was conducted with $\Delta t = 2\pi/240$ until $t = 2400\pi$, which is about 1200 wave periods. During the simulation, it was confirmed that the waves barely change shape and do not break, as monitored by the time series of maximum interface slope $\max(\sqrt{\eta_x^2 + \eta_y^2})$. In all cases listed in table 1, the maximum slope decreased over time and did not exceed its initial value (about 0.2 for AW-ak2 and 0.1 for the rest). In fact, in the AW-ctrl case, the primary harmonic component (wavenumber $(1,0)$ in (x, y) direction) of η explains more than 99.7 % of

the total variance throughout the simulation period, and with the addition of the second harmonic (wavenumber $(2, 0)$), it reaches above $99.998\,\%$.

To demonstrate the accuracy of the present numerical model, the numerical errors are monitored in various ways in the AW-ctrl case, and their time series is shown in figure 2. In figure 2(a), the temporal evolution of error in conserved properties is shown. Water mass conservation can be monitored by the horizontal average of interface elevation, $\bar{\eta}$, and its error is of $O(10^{-16})$. The total x-component momentum M should be conserved in the present set-up because of the free-slip boundary condition at the top and bottom, and the horizontally periodic boundary condition. It is defined as follows:

$$M(t) = r\overline{\int_{-H_o}^{\eta} u\,\mathrm{d}z} + \overline{\int_{\eta}^{H_a} u\,\mathrm{d}z}. \tag{3.1}$$

Here, the overline denotes the horizontal average. The momentum error $\Delta M \equiv M(t) - M(0)$ normalised by initial total momentum is as small as $O(10^{-7})$ after 1200 periods of integration thanks to the full-flux form configuration (2.8). The total energy is calculated as the sum of the kinetic energy (KE) and potential energy (PE):

$$E(t) = r\overline{\int_{-H_o}^{\eta} \frac{1}{2}(u^2 + v^2 + w^2)\,\mathrm{d}z}$$
$$+ \overline{\int_{\eta}^{H_a} \frac{1}{2}(u^2 + v^2 + w^2)\,\mathrm{d}z} + \frac{1}{2}(r-1)g\overline{\eta^2}. \tag{3.2}$$

There is no energy flux through the free-slip top and bottom boundaries, so the temporal change of total energy can be monitored by the viscous dissipation. Therefore, the energy error ΔE can be computed as follows (Tsai & Hung 2007):

$$\Delta E(t) = E(t) - E(0)$$
$$+ \int_0^t \left[\overline{\int_{-H_o}^{\eta} r(uF^x + vF^y + wF^z)\,\mathrm{d}z} + \overline{\int_{\eta}^{H_a} (uF^x + vF^y + wF^z)\,\mathrm{d}z} \right]\,\mathrm{d}t. \tag{3.3}$$

Here, (F^x, F^y, F^z) denotes the viscous force divided by density (as denoted in (2.1a–c)). The time series of energy error normalised with $E(0)$ shows energy growth of $0.01\,\%$ per 1000 wave period, which is sufficiently small even for a long-term integration as in the present problem.

To monitor the mass continuity, the maximum velocity divergence over air and water domains is shown in figure 2(b). It is about $10^{-6\sim-5}$ smaller than the characteristic strain rate by the wave orbital motion. There is a jump of velocity divergence at around $t/2\pi = 150$, which corresponds to the onset of the small-scale flow structure by wave-induced turbulence (§ 4.2). Similarly, the continuity of interface $(w - u\eta_x - v\eta_y)_{z=\eta+0} - (w - u\eta_x - v\eta_y)_{z=\eta-0}$ is confirmed to be small. The numerical error shown in figure 2 is also monitored for the AW-a2 and AW-deepnoise cases and presented in appendix D.

We have also estimated the numerical diffusivity using the W-noturb configuration. At the moment, the tracer equation is not implemented in the two-phase model, so the free-surface model of (Fujiwara *et al.* 2020) that employs identical discretisation was used. Passive tracer with various diffusivity κ and corresponding Péclet number $Pe = \sigma k^{-2}/\kappa$ was placed in the initial field as a vertical water column and was advected and diffused following the wave motion. The same simulation was conducted for a configuration with doubled horizontal and vertical grid points, and the tracer fields at $t = 100\pi$ were
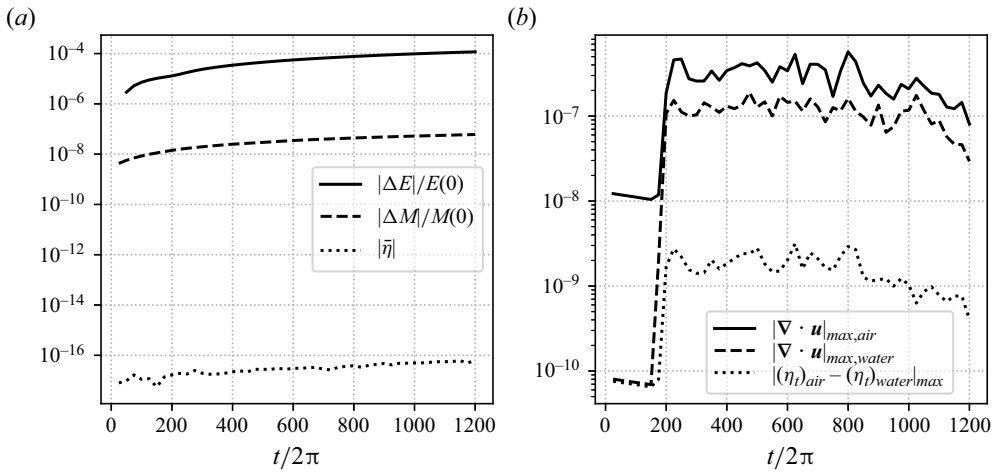
Figure 2. Time series of numerical error in the AW-ctrl case: (*a*) error in total mass, horizontal momentum and energy, as defined in the text; and (*b*) maximum velocity divergence and mass discontinuity at the interface.

compared for the two resolutions. For simulations with $Pe \gtrsim O(10^6)$, the tracer fields were different between the two resolutions, which is dominated by the numerical dispersion and diffusion. However, at $Pe \lesssim O(10^6)$, the simulation results are nearly identical between the two resolutions. Therefore, in the present simulations with $Re_o = 1.5 \times 10^5$, the influence of numerical dispersion/diffusion is negligible.

Finally, to justify the approximation of interfacial velocity by the water-side top layer, the resulting error in interfacial velocity and stress is evaluated in Appendix C between the simulation results of the AW-noturb case. The error between the exact and approximated velocity and the resulting error in momentum and energy exchange between air and water was at most $O(1)\%$. Therefore, its effect on the dynamics reported in the following section is minor.

4. Results

4.1. *Overview of flow structure*

An overview of the simulated wave motion and the resulting turbulence field is presented. Figure 3 is the three-dimensional plot of the streamwise (x component) vorticity component in the AW-ctrl case at $t = 1200\pi$ showing the elongated vortex structure. This is consistent with the streak structure observed in the laboratory experiment by Savelyev *et al.* (2012). The vortices are present both in the water and air domains, but their typical spatial scale is larger in the air side because of the larger kinematic viscosity value there. These turbulent vortices developed over the time scale of $O(100)$ wave periods, as described in § 4.2.

The velocity field in the AW-ctrl case is shown in figures 4 and 5. The instantaneous velocity field is dominated by the wave orbital motion, which is nearly uniform in the y direction, so the deviation from the y average along constant x^* and z^* lines is considered as the turbulence field. Hereinafter, prime is used to denote the turbulence component:

$$\varphi'(x^*, y^*, z^*, t^*) \equiv \varphi(x^*, y^*, z^*, t^*) - \langle \varphi \rangle_y(x^*, z^*, t^*), \tag{4.1}$$
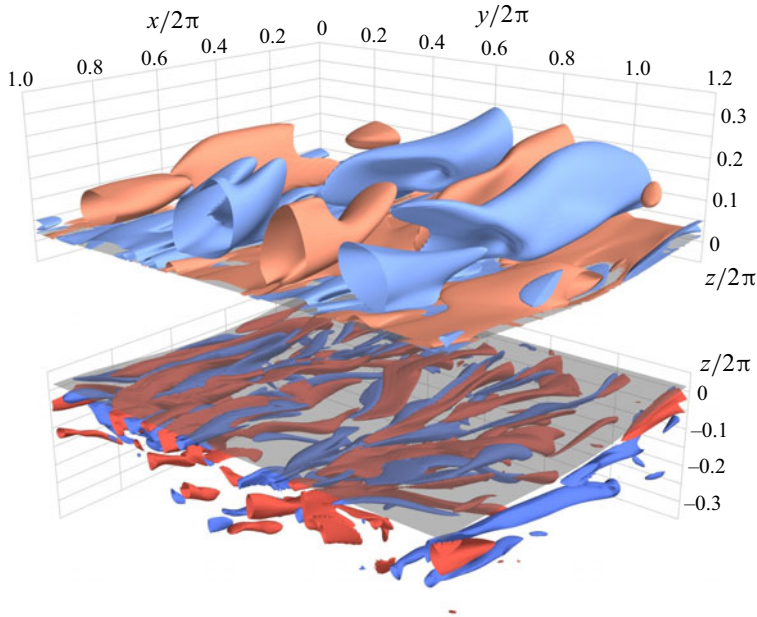
999 A97-16

Figure 3. Three-dimensional plot of the turbulence field of the AW-ctrl case at $t = 1200\pi$. The curved grey surfaces denote the interface, and the air domain is artificially lifted for visibility. Red and blue surfaces denote contours of x-component vorticity $\partial w / \partial x - \partial v / \partial z$ (± 0.013 in the air and ± 0.020 in the water), and the red (blue) surfaces show the positive (negative) contours. Waves propagate towards the x direction.

where φ denotes an arbitrary field and

$$\langle \varphi \rangle_y (x^*, z^*, t^*) \equiv \frac{1}{L_y} \int_0^{L_y} \varphi(x^*, y^*, z^*, t^*) \, \mathrm{d}y^* \qquad (4.2)$$

is the along-crest average.

Figure 4 shows the x–z vertical section of the velocity field at $t/2\pi = 1200$. Since η is almost uniform in the y direction, $\langle \eta \rangle_y$ is used as the interfacial shape. Figure 4(a–c) show that the crest-averaged velocity field is dominated by the wave orbital motion. Although it is invisible in the present plotting, the air-side $\langle u \rangle_y$ sharply adjusts to the water-side value near the interface. This will be further demonstrated in § 4.3. The along-crest variance of velocity components shows that the horizontal components of the turbulence component are located near the interface. The vertical component $\langle w'^2 \rangle_y$ is also concentrated near the interface in the water side, but it is centred at the middle of the domain in the air, representing the large vertical scale of vortices in the air side.

Figure 5 shows the horizontal distribution of u', v' and w' at both air side (upper row, $z^* = 0.2$) and water side (lower row, $z^* = -0.2$). The flow structure is elongated in the wave propagation direction in both the air and water sides, and its spatial scale is finer for the water side because of its smaller viscosity. On the water side, the downwelling part $w' < 0$ is often associated with the down-wave velocity $u' > 0$, which is consistent with the typical structures of the LCs (Leibovich 1983) and the turbulence produced in water-only wave resolving simulations (Tsai *et al.* 2017). The air-side flow shows an upsidedown LC-like structure in that the strong streamwise current region ($u' > 0$) corresponds well with the convergence zone $\partial v' / \partial y < 0$ and the upwelling zone $w' > 0$.
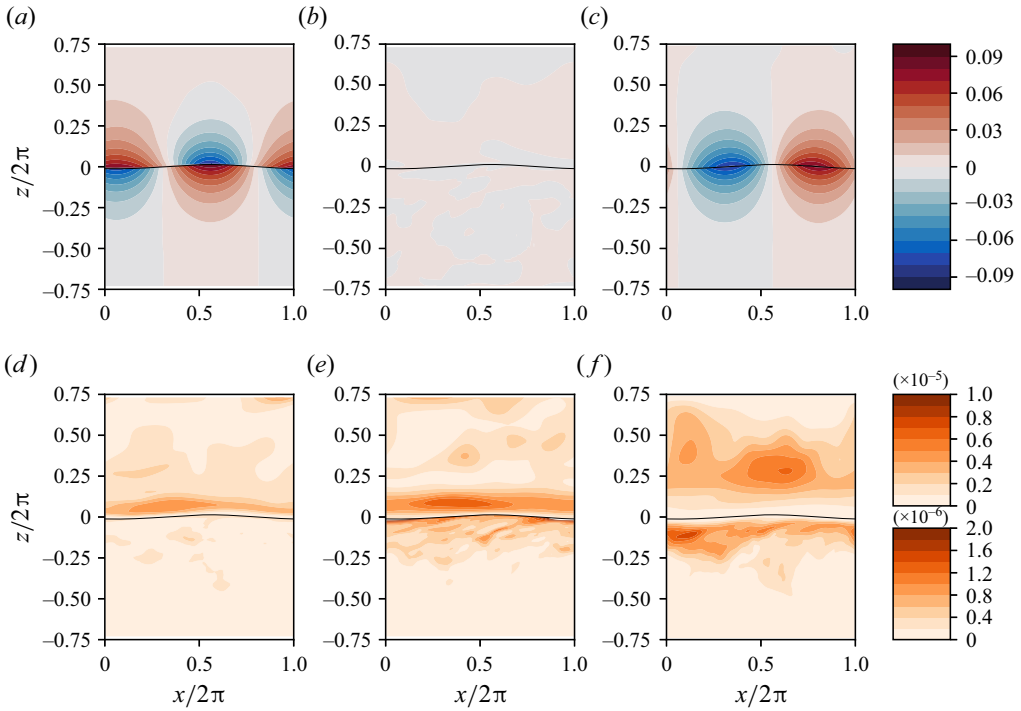
Figure 4. Vertical cross-section of the flow field of the AW-ctrl case at $t = 2400\pi$: (a) $\langle u \rangle_y$; (b) $\langle v \rangle_y$; (c) $\langle w \rangle_y$; (d) $\langle u'^2 \rangle_y$; (e) $\langle v'^2 \rangle_y$; (f) $\langle w'^2 \rangle_y$. Note that the colour range is different for air and water sides in the along-crest variance plots.

This is understandable because the wave-driven airflow (figure 7d) has the negative shear $\partial \bar{u}^E / \partial z < 0$, and the shear of the air-side Stokes drift $\partial u^{St} / \partial z = -2a^2 e^{-2z} < 0$ has the same sign. This results in CL2 instability (Leibovich 1983), producing the roll structure in the air side as well. The W-ctrl case also showed a turbulent flow pattern similar to the water side of the AW-ctrl case, and their difference in turbulence intensity is discussed in § 4.2.

4.2. *Temporal evolution of flow field*

Here, the temporal evolution of the flow field is described. First, figure 6 shows the temporal variation of the wave amplitude. The wave amplitude is evaluated as $a(t) = (2\overline{\eta^2})^{1/2}$, where the overline denotes horizontal average. Both in the AW and W cases, the decay rate is almost identical with and without turbulence. The simulated decay rate followed the linear theory of Dore (1978) (AW) and Lamb (1932) (W) well, indicating the prevalence of linear dynamics. The simulated decay rate of both the AW-ctrl and AW-noturb cases exceeded the theoretical prediction slightly, although this deviation diminished with a higher vertical resolution near the interface on the air side. This suggests that the air-side Stokes layer is playing a central role in the energy dissipation, and it needs to be properly resolved when we focus on its role. With that caveat in mind, we proceed with the present resolution, as the enhanced wave decay predicted by the linear theory is mostly reproduced.

As waves decay, they give up the horizontal momentum and produce a vortical current, namely, the Eulerian mean drift. The Eulerian mean drift is evaluated by first vertically
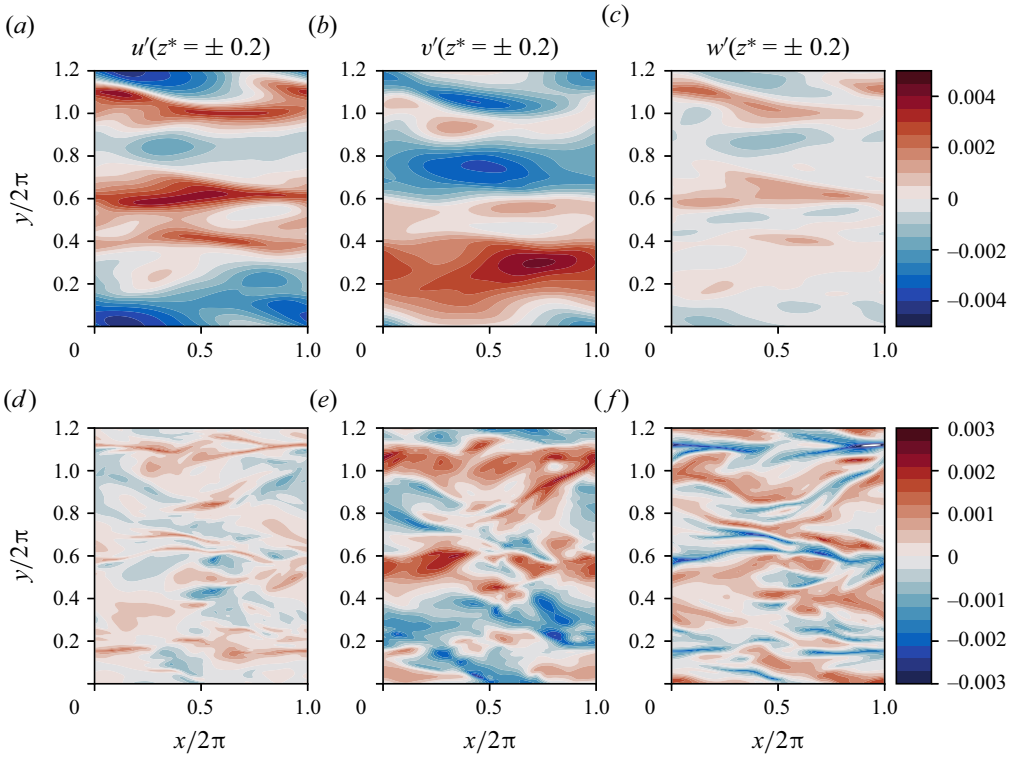
Figure 5. Top view of u', v' and w' obtained in the AW-ctrl case at $t = 2400\pi$: $(a$–$c)$ distributions on $z^* = 0.2$ (air) and $(d$–$f)$ distributions on -0.2 (water).
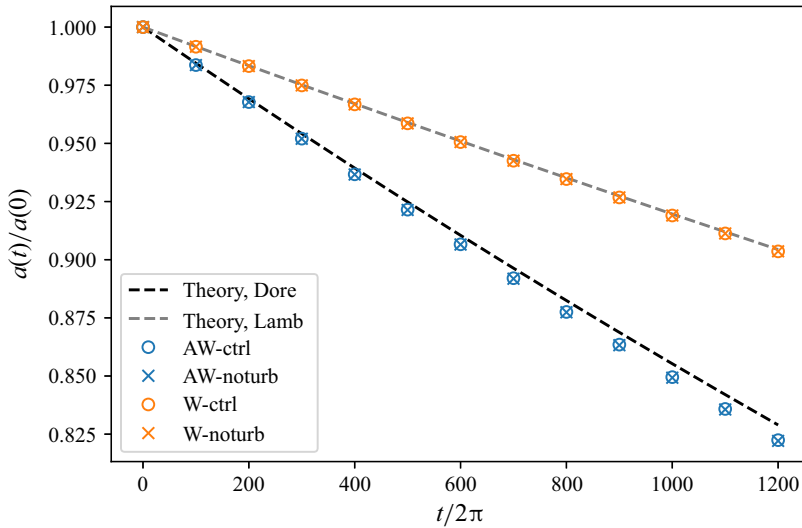

Figure 6. Temporal change of wave amplitude $a(t) = \sqrt{2\overline{\eta^2}}$ normalised with its initial value $a(0)$. Dashed lines denote the decay rate predicted with the linear theories (1.3) and (1.1).
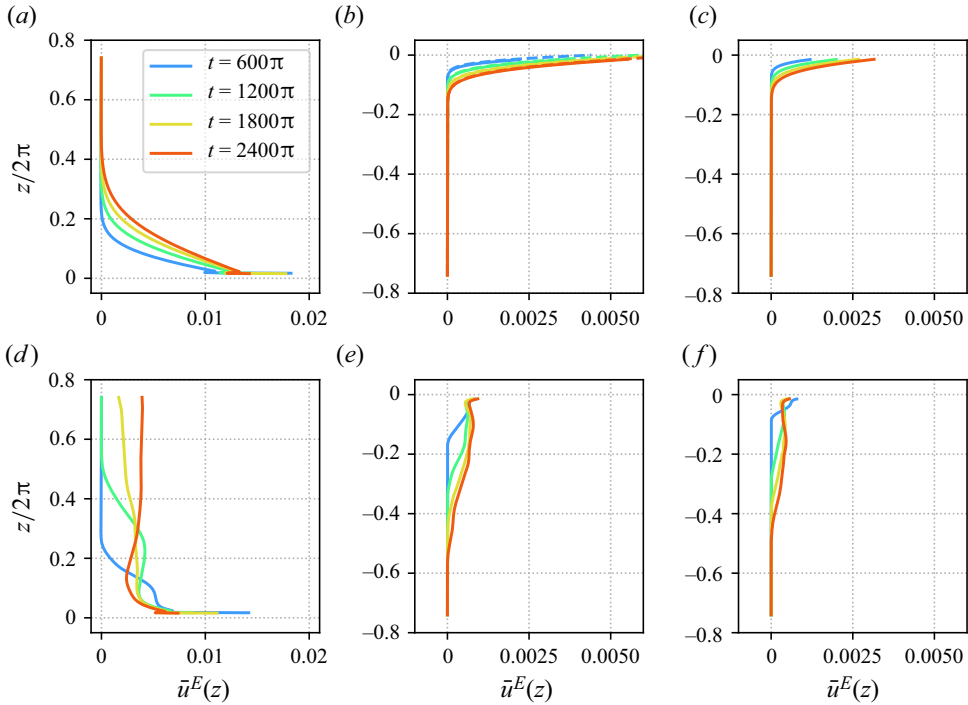
Figure 7. Vertical profiles of the Eulerian mean horizontal velocity $\bar{u}^E$ of the AW-noturb, AW-ctrl, W-noturb and W-ctrl cases: (*a*) AW-noturb, air; (*b*) AW-noturb, water; (*c*) W-noturb; (*d*) AW-ctrl, air; (*e*) AW-ctrl, water; (*f*) W-ctrl. Dashed lines in (*b*) show the result of the one-dimensional diffusion equation (4.3).

interpolating the horizontal velocity field u to fixed levels and then taking a horizontal average. The temporal evolution of the Eulerian mean horizontal velocity $\bar{u}^E(z, t)$ is shown in figure 7. The data at the vertical levels between wave crests and troughs are not plotted here. The comparison of the AW-noturb and W-noturb cases (figure 7*b*,*c*) shows that, due to the enhanced energy decay in the air–water coupling, the development of $\bar{u}^E$ is also accelerated in the AW case. In the air side of the AW-noturb case (figure 7*a*), the Eulerian mean drift develops in the down-wave direction. The drift near the interface is stronger than that in the water-side drift. However, its velocity scale is still on the order of the water-side Stokes drift $O(a^2 k \sigma)$. In the realistic ocean, this is likely significantly smaller than that of the wind over the waves, which is typically on the order of the wave phase speed $O(\sigma/k)$.

The evolution of water-side Eulerian mean drift in the AW-noturb case is compared with the virtual wave stress theory. The one-dimensional diffusion equation below was simulated for the velocity profile $u(z, t)$ in the water side ($-H_o \leq z \leq 0$):

$$\frac{\partial u}{\partial t} = \nu_o \frac{\partial^2 u}{\partial z^2}. \tag{4.3}$$

The upper boundary condition is provided as the virtual wave stress, $\nu_o(\partial u/\partial z) = \tau_{ao}^{vws}$ (1.4), and the bottom boundary is assumed as free-slip. Since the amplitude time series was well followed by the linear theory (figure 6), the wave amplitude $a(t)$ used in τ_{ao}^{vws} is assumed to exponentially decay with time as $a(t) = a(0)e^{-\gamma_{ao}t}$. The result is shown
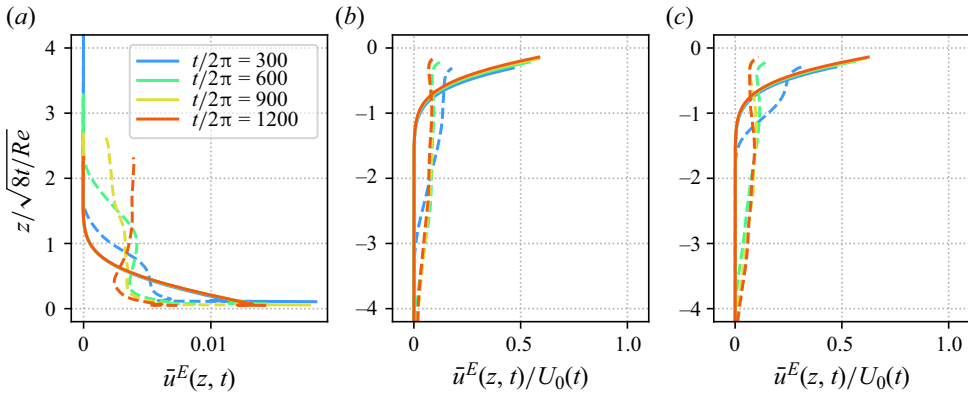
999 A97-20

Figure 8. Vertical profiles of the normalised Eulerian mean horizontal velocity $\bar{u}^E$ of the AW-noturb, AW-ctrl, W-noturb and W-ctrl cases: (*a*) air-side velocity profile in the AW cases; (*b*) water-side profile in the AW cases; and (*c*) water-side profile in the W cases. Solid (dashed) lines in each panel indicate the AW-noturb and W-noturb (AW-ctrl and W-ctrl) cases. Vertical coordinate is normalised with the viscous length scale $\sqrt{t/Re}$. The horizontal velocity is normalised with $U_0(t)$ of (4.4) in (*b,c*).

as the dashed lines in figure 7(*b*), which mostly overlaps with the AW-noturb simulation result.

In the three-dimensional cases, turbulence alters the velocity profile by carrying horizontal momentum away from the interface. As a result, velocity profile $\bar{u}^E$ shows weaker vertical shear in both air and water sides (figure 7*d–f*).

Veron & Melville (2001) derived a similarity solution of the wind-driven sheared current in the water-side based on the one-dimensional diffusion equation (4.3) subject to a constant wind stress τ. Wu & Deike (2021) conducted a two-dimensional DNS of the wind–wave growth under the influence of viscosity and confirmed that the wind-induced drift current $\bar{u}^E(z,t)$ falls into a single curve if the depth and the velocity are scaled with $\sqrt{\nu_o t/8}$ (under our non-dimensionalisation $\sqrt{t/8Re_o}$) and $U_0(t) \equiv \bar{u}^E(0,t)$, respectively. Figure 8(*b,c*) show the temporal evolution of the Eulerian current profile scaled as previously. Here, the velocity scale $U_0(t)$ is evaluated as (Veron & Melville 2001; Wu & Deike 2021)

$$U_0(t) = \frac{2}{\sqrt{\pi}} \tau \sqrt{\frac{t}{Re_o}}, \qquad (4.4)$$

and $\tau = \tau_{ao}^{vws}(0)$ and $\tau = \tau_o^{vws}(0)$ for the AW-ctrl/noturb and W-ctrl/noturb cases, respectively. The AW-noturb and W-noturb cases follow the scaling well, but in the AW-ctrl and W-ctrl cases, the shear is reduced due to turbulence, and the drift current profiles deviate from the scaling solution.

On the air side, however, the drift velocity scales differently. The Eulerian current profile in the air with vertical coordinate scaled with $\sqrt{t/8Re_a}$ is shown in figure 8(*a*). Unlike on the water side, the profiles of the AW-noturb case fall into a single curve without scaling with $U_0(t)$. Therefore, the air-side drift current develops as if a Dirichlet-type boundary condition is imposed at the bottom.

Next, the temporal evolution of turbulence, characterised by deviation velocity from y average (u', v', w') is compared among cases. Figure 9 shows the temporal evolution of water-side turbulent kinetic energy (TKE) and the spanwise wavelength l_s. TKE is defined as $(r/2)(u'^2 + v'^2 + w'^2)$. Temporal evolution of its vertical profile (horizontally averaged
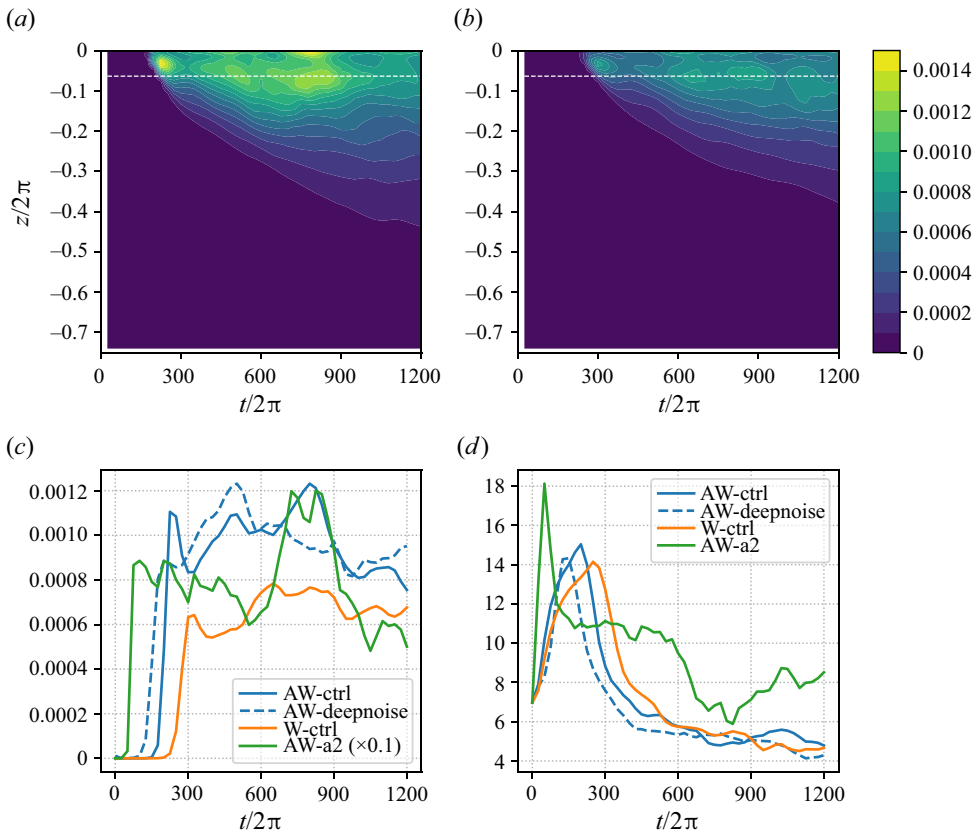
Figure 9. Temporal evolution of water-side turbulence statistics in the AW-ctrl, W-ctrl, AW-deepnoise and AW-ak2 cases: (*a,b*) vertical-temporal distribution of horizontally averaged TKE in the AW-ctrl and W-ctrl cases, respectively; (*c*) time series of TKE averaged over $-0.4 \le z^* \le 0$, where the TKE of the AW-2d case is multiplied by 0.1 for visibility; (*d*) time series of spanwise wavenumber l_s defined in (4.5) evaluated at $-0.4 \le z^* \le 0$. Horizontal white-dashed lines in (*a,b*) denote $z^* = -0.4$ above which the TKE and l_s in (*c,d*) are evaluated.

along z^*-surface) is shown for the AW-ctrl (figure 9*a*) and W-ctrl (figure 9*b*) cases. Turbulence arises from the near-interface layer and spreads into the water as time passes. The magnitude of turbulence is greater in AW-ctrl than in W-ctrl throughout the simulation period. Note that, even at $t/2\pi = 1200$, the turbulence has not fully reached the bottom of the water side. However, the turbulence near the interface has reached a mature stage, and the turbulence statistics no longer change rapidly. Therefore, we can expect that the flow field of AW-ctrl after $t/200\pi \approx 500$ would well reflect the dynamics of turbulence produced by persistent wave forcing in the air–water coupled configuration.

To illustrate the turbulence development in different cases more quantitatively, let us examine TKE vertically averaged over $-0.4 \le z^* \le 0$ shown in figure 9(*c*). In all cases, the TKE is initially of very small magnitude (e.g. $O(10^{-7})$ in AW-ctrl), rapidly grows in the earlier stage, and then saturates, reflecting some instability mechanism at work. The onset of instability is quicker in AW-ctrl ($t/2\pi \approx 175$) than W-ctrl ($t/2\pi \approx 250$), and TKE magnitude of the former remains stronger than the latter throughout the simulation period. Therefore, the air–water coupling enhances the wave-induced turbulence.

999 A97-22

To characterise the spatial scale of the turbulence, we have evaluated the TKE-weighted mean spanwise wavenumber l_s following Tsai *et al.* (2017), as follows:

$$l_s(t) = \frac{\int l S(l, t)\, \mathrm{d}l}{\int S(l, t)\, \mathrm{d}l}, \tag{4.5}$$

where l is the wavenumber in the y direction and $S(l, t)$ is the spanwise power spectral density of turbulence velocity averaged over $0 \leq x^* \leq 2\pi$ and $-0.4 \leq z^* \leq 0$,

$$S(l, t) = \frac{1}{0.4} \frac{1}{2\pi} \int_0^{2\pi} \int_{-0.4}^0 [S_u(x^*, l, z^*, t) + S_v(x^*, l, z^*, t) + S_w(x^*, l, z^*, t)]\, \mathrm{d}z^*\, \mathrm{d}x^*, \tag{4.6}$$

where S_u and so on denote the power spectral density obtained by applying the Fourier transform in the y^* direction.

The temporal evolution of l_s is shown in figure 9(*d*). Before the onset of instability, the turbulence field is dominated by the spatial scale of $l_s \approx 7$, which corresponds to the initial noise field. As the disturbance grows, vortices with relatively high wavenumbers first develop, and then the dominant spanwise scale grows (l_s decreases) rapidly after the instability is saturated. At a later stage of the simulation period, the temporal development of l_s is small. The AW-ctrl and W-ctrl cases show the similar temporal evolution of l_s, except that the time series in W-ctrl is lagged behind AW-ctrl by about 50 periods, consistent with the delay of the instability onset.

The result of the AW-deepnoise case is shown in figure 9(*c*,*d*) with a blue dashed line. The rapid growth of TKE at the onset stage and the subsequent decrease of l_s observed in the AW-deepnoise case precedes the corresponding changes in AW-ctrl. As a result of the initial noise injected into all the water grid points, the initial TKE level (about 1×10^{-5}) is about 300 times greater than in the AW-ctrl case. This results in an enhancement of the initial amplitude of the fastest-growing mode, so we can understand that the onset of instability occurs earlier. However, after the turbulence reached maturity, there was no clear difference between AW-deepnoise and AW-ctrl. Therefore, the statistical features of the simulated turbulence are not dependent on the initial noise structure, and only the onset timing of instability is changed.

To examine the influence of wave amplitude on the phenomenon, we have conducted an air–water coupled case with greater initial wave amplitude, $a = 0.2$ (AW-a2 case). The spatial structure of turbulent velocity was similar to AW-ctrl: the vortices elongated in wave-propagation direction was observed, and the temporal evolution of turbulence statistics is shown in figure 9. Overall, the temporal evolution of turbulence is similar to the AW-ctrl case, but the onset of instability is earlier ($t/2\pi \approx 75$). This reflects the stronger Eulerian sheared current ($\propto \tau_{ao}^{vws} \propto a^2$) than AW-ctrl, resulting in a greater growth rate of instability. The magnitude of TKE at the mature stage (average over $600 \leq t/2\pi \leq 1200$) is about eight times greater than that of AW-ctrl.

From these results, we can make a remark on the onset time scale of wave-induced turbulence (300 periods in the AW-ctrl case). The DNS by Tsai *et al.* (2017) required only 10 wave periods for turbulence to develop. In their set-up, the wave slope was 0.25, which is even greater than in our AW-a2 case, and they imposed the initial noise that contains 0.1 % of the total energy. The large amplitude should lead to a strongly unstable condition, and the fraction of disturbance energy is much greater than our set-up ($O(10^{-6})$% for the AW-ctrl and AW-a2 cases), so the initial instability is considered to be strongly seeded. Therefore, in the simulation set-up of Tsai *et al.* (2017), the instability is expected to arise

at an early stage after the simulation starts. Notably, the tank experiment of Savelyev *et al.* (2012) also observed the turbulence growth at a similar time scale (ramp-up time of 7–10 periods followed by 6–9 periods with constant wave amplitude). Therefore, we consider that the initial noise field of our simulation design was too weak, leading to unrealistically long spinup period of $O(100)$ wave periods. However, our simulations demonstrate that the flow field is inherently unstable and the turbulence develops over time even with such a small initial disturbance.

4.3. *Momentum and KE budget analysis*

To examine the mechanism of vertical transfer of momentum and energy, the budget equations of the horizontal momentum and KE were explored. The analysis was conducted on the model coordinate z^* as in preceding studies using wave resolving simulations (Sullivan *et al.* 2008; Cao & Shen 2021). In our framework, the horizontally averaged x-component momentum equation is written as follows:

$$\frac{\partial}{\partial t^*}(\overline{\rho h u}) = -\frac{\partial}{\partial z^*}(F_p + F_v + F_a), \tag{4.7}$$

where the overline denotes the horizontal average along constant z^*. Here F_p, F_v and F_a denote the vertical flux of horizontal momentum by form stress, viscous stress and advection, respectively, and are defined as follows:

$$F_p = \overline{\tilde{p} z_{x^*}}, \tag{4.8a}$$

$$F_v = -\rho \overline{h(T^{xz} - z_{x^*} T^{xx} - z_{y^*} T^{xy})}, \tag{4.8b}$$

$$F_a = \rho \overline{h \omega u}. \tag{4.8c}$$

Here, $\omega \equiv h^{-1}(w - z_{t^*} - u z_{x^*} - v z_{y^*}) = \Omega/h$ is the z^* velocity. The density ρ and total pressure $\tilde{p}$ are non-dimensionalised with the air density, i.e. $\rho = 1$ in the air and r in the water. Note that the forecast variable of (4.7) is the layer-thickness-weighted momentum $\overline{h u}$, which includes the momentum associated with both the wave motion and the vortical current. The budget equation of the KE $E \equiv \rho(u^2 + v^2 + w^2)/2$ can be obtained by taking an inner product of (2.8a–c) and (u, v, w):

$$\frac{\partial}{\partial t^*}(\rho \overline{h E}) = -\frac{\partial}{\partial z^*}(W_p + W_v + W_a) - C - D. \tag{4.9}$$

Here W_p, W_v and W_a are the vertical flux of KE by pressure, viscous stress and advection, respectively, C is the conversion term to PE, and D is the dissipation. They are defined as follows:

$$W_p = \overline{\tilde{p}(z_{t^*} + h\omega)} = \overline{\tilde{p}(w - z_{x^*} u - z_{y^*} v)}, \tag{4.10a}$$

$$W_v = -\rho \left[\overline{h u(T^{xz} - z_{x^*} T^{xx} - z_{y^*} T^{xy})} \right.$$
$$+ \overline{h v(T^{yz} - z_{x^*} T^{yx} - z_{y^*} T^{yy})}$$
$$+ \left. \overline{h w(T^{zz} - z_{x^*} T^{zx} - z_{y^*} T^{zy})} \right], \tag{4.10b}$$

$$W_a = \overline{h\omega E}, \tag{4.10c}$$

$$C = \rho\overline{hw} = \rho\left[\frac{\partial}{\partial t^*}(\overline{hz}) + \frac{\partial}{\partial z^*}(\overline{h\omega z})\right], \tag{4.10d}$$

$$D = (2\rho/Re)\overline{hS^{ij2}}. \tag{4.10e}$$

Here, $S^{ij} = (\partial u_i/\partial x_j + \partial u_j/\partial x_i)/2$ is the strain rate. The PE conversion term C can be decomposed into the local PE increment $\rho\partial(\overline{hz})/\partial t^*$ and the vertical flux of PE $\rho\partial(\overline{h\omega z})/\partial z^*$ (the right-hand side of (4.10d)), but we only evaluate their total effect. In the following analysis, the momentum and KE budget equation terms are evaluated as temporal averages over $600 \le t/2\pi \le 1200$.

To separate the influence of wave motions and turbulence, the flux terms in (4.8) and (4.10) are decomposed based on horizontal harmonics. An arbitrary variable $\varphi(x^*, y^*, z^*)$ is expanded in the Fourier series:

$$\varphi(x^*, y^*, z^*) = \sum_{l=-N_x/2-1}^{N_x/2} \sum_{m=-N_y/2-1}^{N_y/2} \hat{\varphi}_{lm}(z^*) \exp\mathrm{i}\left(\frac{2\pi l x^*}{L_x} + \frac{2\pi m y^*}{L_y}\right). \tag{4.11}$$

Here, i denotes the imaginary unit, N_x and N_y are the number of grid points in x and y direction, respectively. Since φ is a real function, the Fourier coefficients satisfy the relation $\hat{\varphi}_{-l\,-m} = \hat{\varphi}_{lm}^{\star}$, where the superscript $\star$ denotes complex conjugate.

Then, a flux composed of a product of two variables A, B can be written as follows:

$$\overline{AB} = \sum_{l=-N_x/2+1}^{N_x/2} \sum_{m=-N_y/2+1}^{N_y/2} \hat{A}_{lm}\hat{B}_{lm}^{\star} = \hat{A}_{00}\hat{B}_{00}^{\star} + 2\mathrm{Re}[\hat{A}_{10}\hat{B}_{10}^{\star}] + \cdots. \tag{4.12}$$

Here, Re denotes the real part. Since the leading-order wave motion arises in the wavenumber $(l, m) = (1, 0)$, the rectified wave effect is expected to arise mainly in the $\hat{A}_{10}\hat{B}_{10}^{\star}$ term. We first assessed the contribution of major harmonic components to total flux in the wave-only (AW-noturb) case and then compared the result with AW-ctrl.

First, the first harmonic coefficients of u, w and $\tilde{p}$ in the AW-noturb case were investigated to obtain an overview of the wave-induced variation. For an instantaneous field φ, its first harmonic $\hat{\varphi}_{10}$ is separated into the in-phase ($\hat{\varphi}_r$) and quadrature ($\hat{\varphi}_i$) parts relative to the surface elevation η as follows:

$$\hat{\varphi}_r = \mathrm{Re}\left[\hat{\varphi}_{10}/(\hat{\eta}_{10}/|\hat{\eta}_{10}|)\right], \hat{\varphi}_i = \mathrm{Im}\left[\hat{\varphi}_{10}/(\hat{\eta}_{10}/|\hat{\eta}_{10}|)\right]. \tag{4.13}$$

The vertical profile of in-phase and quadrature part of $\hat{u}_{10}$, $\hat{w}_{10}$ and $\hat{\tilde{p}}_{10}$ in the AW-noturb case are shown in figure 10. There, the in-phase part of pressure $\hat{\tilde{p}}_r$ is not shown because it does not contribute to the momentum and KE flux. These coefficients are evaluated as the composites during $600\pi \le t < 602\pi$. Following Cao & Shen (2021), the coefficients are categorised into major and minor components. Here, $\hat{u}_r$, $\hat{w}_i$ and $\hat{\tilde{p}}_r$ are the major components that are present even in the inviscid interfacial waves, and the minor components arise due to the viscosity and the interaction with Eulerian current.

The harmonic coefficient profiles consist of two parts, namely, the SBL and the bulk region. The SBL is the region near the interface where an oscillatory response to the boundary condition is present, and its e-folding thicknesses in the air and water sides are $\sqrt{2/Re_a} \approx 1.8 \times 10^{-3} \times 2\pi$ and $\sqrt{2/Re_o} \approx 5.8 \times 10^{-4} \times 2\pi$, respectively. Figure 10
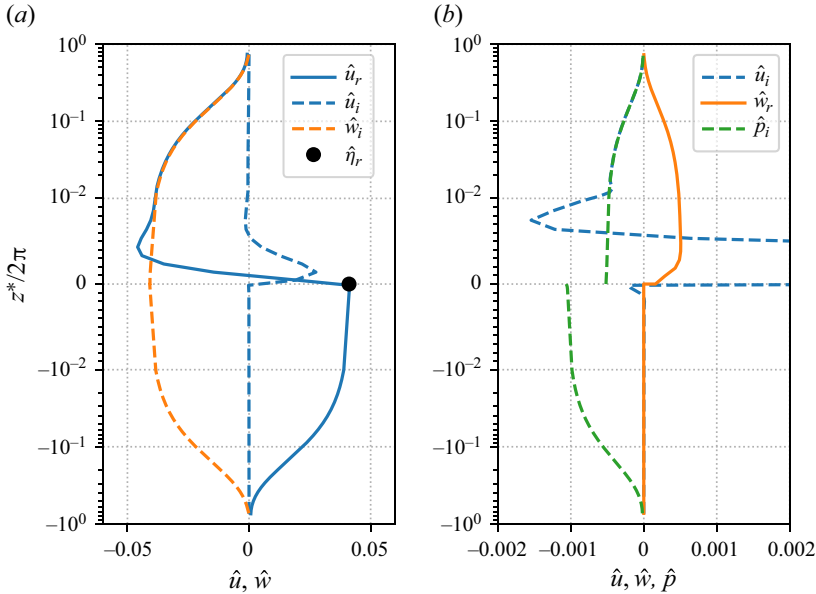
(a)

(b)

Figure 10. Vertical profiles of the first harmonic coefficients of u, w and p in the AW-noturb case: (*a*) profiles of the major parts; and (*b*) profiles of the minor parts. The profile of $\hat{u}_i$ is shown in both panels. The vertical axis is logarithmic for $|z^*/2\pi| \geq 10^{-2}$ and linear for $|z^*/2\pi| < 10^{-2}$.

shows that the response to the boundary is visible to the extent approximately five times thicker than those values. Therefore, we loosely define the SBL of air and water as $0 \leq z^*/2\pi \leq 0.01$ and $-0.003 \leq z^*/2\pi \leq 0$, respectively, and the region outside them as the bulk region.

The water-side profile of $\hat{u}_{r,i}$ and $\hat{w}_{r,i}$ are mostly consistent with the irrotational waves: u is in-phase and w is $90°$ out-of-phase with η, and their minor components are nearly zero. In water-side SBL, $\hat{u}_i$ shows a slight deviation from zero, which is the response to satisfy the no-slip interfacial boundary condition, whereas $\hat{w}_r$ is nearly zero throughout the water side. The phase of $\tilde{p}$ is slightly ahead of η (higher pressure at the forward face of the wave). In the air-side bulk region, the major components $\hat{u}_r$ and $\hat{w}_i$ agree with the irrotational waves. However, the minor components $\hat{u}_i$ and $\hat{w}_r$ show greater deviation than the water side. From figure 10, it can be seen that $\hat{u}_r\hat{w}_r + \hat{u}_i\hat{w}_i \approx 0$, so u and w are still in quadrature. In the air-side SBL, there is a strong SBL response due to the no-slip boundary condition and large density ratio ρ_o/ρ_a, resulting in a strong shear layer just above the interface. As in the water side, the phase of $\tilde{p}$ is slightly ahead of η.

The momentum flux profile of the AW-noturb case is shown in figure 11(*a*). In the water side, the net momentum flux $F_p + F_v + F_a$ is upwards with a maximum value at $z^*/2\pi \approx -0.08$. Therefore, the horizontal momentum is transferred from the lower part to the near-surface part of the water body. This corresponds to the transformation of the horizontal momentum from the wave motion that is distributed over the vertical scale of $O(0.5)$, to the vortical current that diffuses downwards from the SBL. The upwards momentum transfer in the bulk of the water is performed via the form stress and the advection, and the viscous stress carries momentum downwards. Each term is decomposed into contributions from harmonics, and it is found that the following terms dominate the momentum flux terms:

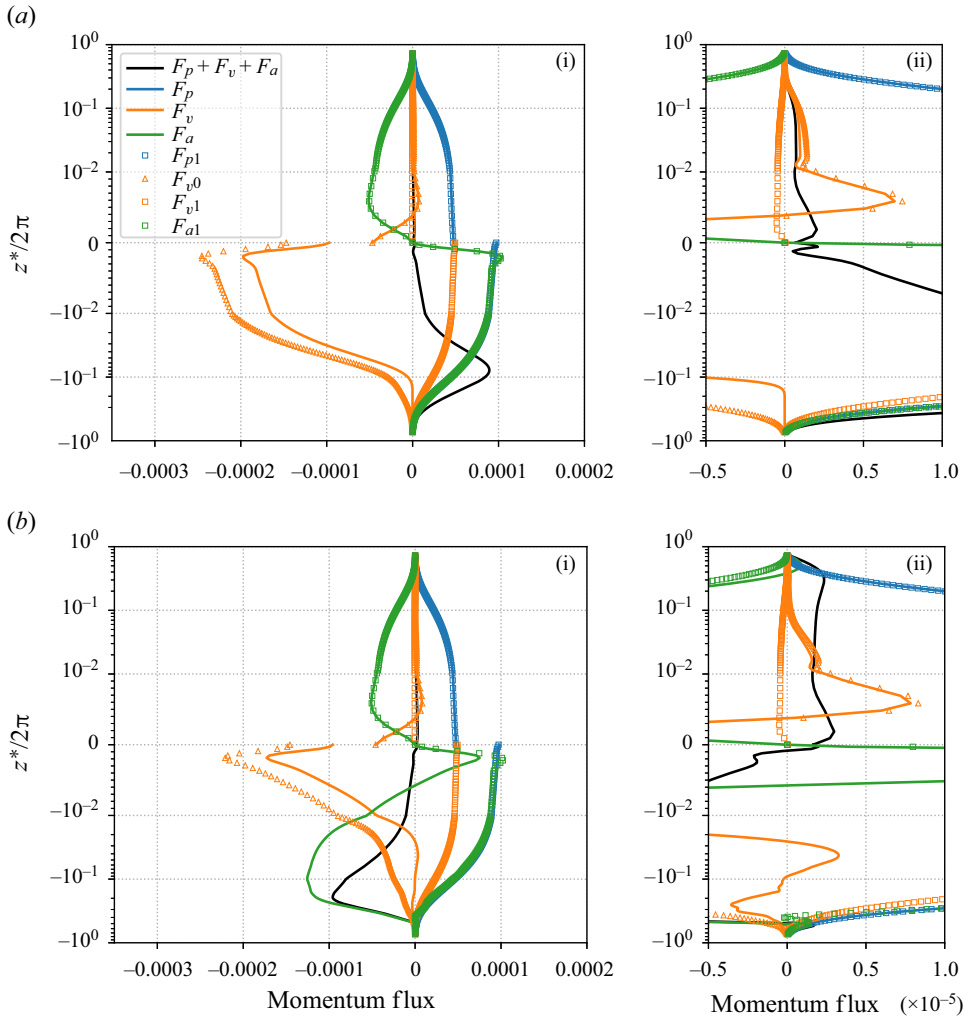$$F_{p1} = 2\mathrm{Re}[\hat{\tilde{p}}_{10}\hat{z}^{\star}_{x^*10}], \qquad (4.14a)$$

Figure 11. Vertical profiles of the momentum flux components defined in (4.8): (*a*,*b*) profiles of the AW-noturb and AW-ctrl cases, respectively; (*a* ii,*b* ii) the same quantities as in (*a* i,*b* i), but the range of the horizontal axis is magnified. The vertical axis is logarithmic for $|z^*/2\pi| \geq 10^{-2}$ and linear for $|z^*/2\pi| < 10^{-2}$.

$$F_{v0} = \rho \hat{T}_{00}^{xz}, \quad F_{v1} = -2\rho \mathrm{Re}[\hat{T}_{10}^{xx} \hat{z}_{x^*10}^{\star}], \tag{4.14b}$$

$$F_{a1} = 2\rho \mathrm{Re}[\hat{u}_{10} \hat{\omega}_{10}^{\star}]. \tag{4.14c}$$

These terms are plotted in figure 11(*a*) as markers. The pressure form stress is caused by the relative phase shift of $\tilde{p}$ and z. Note that z is in phase with η by the model coordinate definition, so $\mathrm{Re}[\hat{\tilde{p}}_{10}\hat{z}_{x^*10}^{\star}] \propto \hat{\tilde{p}}_i \hat{\eta}_r$, and this correlation is consistent with that observed in figure 10. The viscous stress is composed of two components, out of which the downwards momentum transfer is supported by the phase-independent stress term $\hat{T}_{00}^{xz} = \overline{T^{xz}}$. This is an understandable result considering that the development of the vortical current is well-reproduced in the one-dimensional wave-averaged equation with the momentum imposed as the uniform virtual wave stress at the surface.

In the air side, the momentum is transferred upwards from the near-interface layer to the bulk of the air. The upwards transfer of momentum roughly agrees with the viscous stress, where the phase-independent part $\hat{T}_{00}^{xz} = \overline{T^{xz}}$ plays a central role as in the water side. The pressure and advective momentum fluxes almost cancel each other.

The discussed results are compared with the momentum transfer profile in the presence of turbulence (AW-ctrl), as depicted in figure 11(*b*). In contrast to the AW-noturb case, the momentum is transferred downwards in the water side. This is because, over $600 \leq t/2\pi \leq 1200$ of the AW-ctrl case, the Eulerian current profile (figure 7*e*) developed deeper than the vertical extent of the wave momentum ($z^* \gtrsim -0.5$) due to the presence of turbulence. This is illustrated in the significant difference in F_a from AW-noturb. Although the contribution from the first harmonic (F_{a1}) is almost unchanged, the turbulent flow structure that arises at other horizontal wavenumbers carries momentum downwards to change the direction of total advective momentum flux in the bulk of the water side. Due to the reduced vertical shear of the horizontal velocity, the downwards momentum transfer by viscosity (F_v) is also reduced. The pressure-induced momentum transfer is almost unchanged. Although somewhat mild, the change from AW-noturb is also visible in the air side especially away from the interface ($z^*/2\pi \leq 0.1$). There, the upwards momentum transfer is intensified compared with the AW-noturb case, and this difference can be attributed to the advective flux. As in the water side, the contribution from the first harmonic is unchanged, and the turbulence influence at other components enhances the upwards momentum transfer.

In both the AW-ctrl and AW-noturb cases, the magnitude of net momentum transfer between air and water is much smaller than that within the water layer. Therefore, most of the horizontal momentum lost from the waves is received as the water-side vortical current that diffuses downwards from the SBL. Since the cross-z^* velocity ω is zero at the interface by definition, the cross-interface momentum flux is done by the pressure and viscous stresses. At both the air and water sides, the pressure–slope correlation carries momentum upwards, whereas the viscous stress nearly cancels that. Although small, the net momentum flux across the interface was upwards in this case.

The profile of KE source terms and the KE tendency in the AW-noturb case is shown in figure 12(*a*). The profile of the dissipation differs significantly between the air and water sides. In the air side, strong dissipation occurs in the SBL, whereas the dissipation in the water side occurs over the bulk of the water. The vertically integrated dissipation in the air and water was 9.362×10^{-5} and 1.009×10^{-4}, respectively. The dissipation term is decomposed into harmonics, and the contribution from the first harmonic, D_1 defined as follows, is found to account for most of the total dissipation:

$$D_1 = (2\rho/Re)\overline{\left(|\hat{S}_{10}^{xx}|^2 + 2|\hat{S}_{10}^{xz}|^2 + |\hat{S}_{10}^{zz}|^2\right)}. \tag{4.15}$$

The vertical profile of the PE conversion is less straightforward to interpret, but their vertically integrated value in the air and water is 2.22×10^{-7} and -9.80×10^{-5}, respectively. The PE-to-KE conversion in the water is concentrated in the SBL, as the integral of C over $-0.005 \leq z^*/2\pi \leq 0$ accounts for 98.4 % of the total. The tendency of KE $\mathrm{d}(\overline{hE})/\mathrm{d}t^*$ mostly consists of water-side contribution due to the large density ratio, and its vertical structure corresponds to the wave orbital motion. Vertically integrated KE tendency in the air and water is -9.81×10^{-8} and -9.72×10^{-5}, respectively. The total energy loss (vertically integrated $-C - \partial(hE)/\partial t^*$) in the air and water is -1.24×10^{-7} and 1.95×10^{-4}, respectively. Therefore, most of the energy lost during the wave attenuation originates from the water side, but approximately half of it is transferred to and dissipated in the air-side SBL. Considering the relative contribution of energy
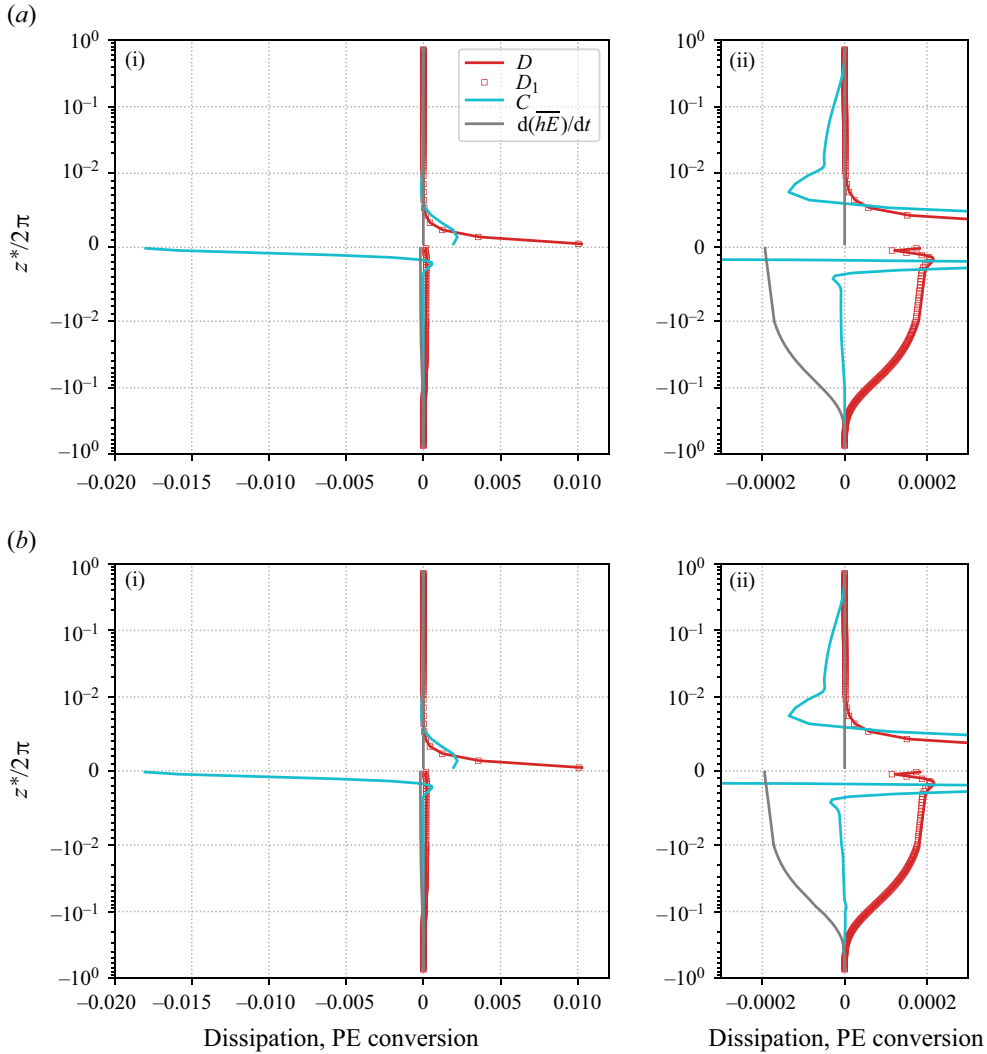
Figure 12. Vertical profiles of the dissipation and PE conversion terms defined in (4.10): (a,b) profiles of the AW-noturb and AW-ctrl cases, respectively; (a ii,b ii) the same quantities as in (a i,b i), but the range of the horizontal axis is magnified. Note that the positive values correspond to the KE sink and *vice versa*. The vertical axis is logarithmic for $|z^*/2\pi| \geq 10^{-2}$ and linear for $|z^*/2\pi| < 10^{-2}$.

dissipation in the air and water (1.3), the fraction above would increase with higher Reynolds number, i.e. longer waves.

The KE flux terms in the AW-noturb case are shown in figure 13(a). In the air side, the pressure flux term carries KE downwards to the air-side SBL, where strong dissipation occurs. Due to the large density ratio, the viscous and advective flux terms contribute little to the total KE flux. In the bulk of the water, KE is transferred upwards by the pressure term and downwards by the viscosity term, resulting in a net downwards flux. In the near-surface water, however, the downwards viscous energy flux sharply approaches zero, resulting in a net upwards energy flux. This supplies energy to the air-side SBL, where the energy is strongly dissipated. Although most of the energy flux is explained with pressure and viscous terms, advective energy flux is also present in both domains, carrying energy
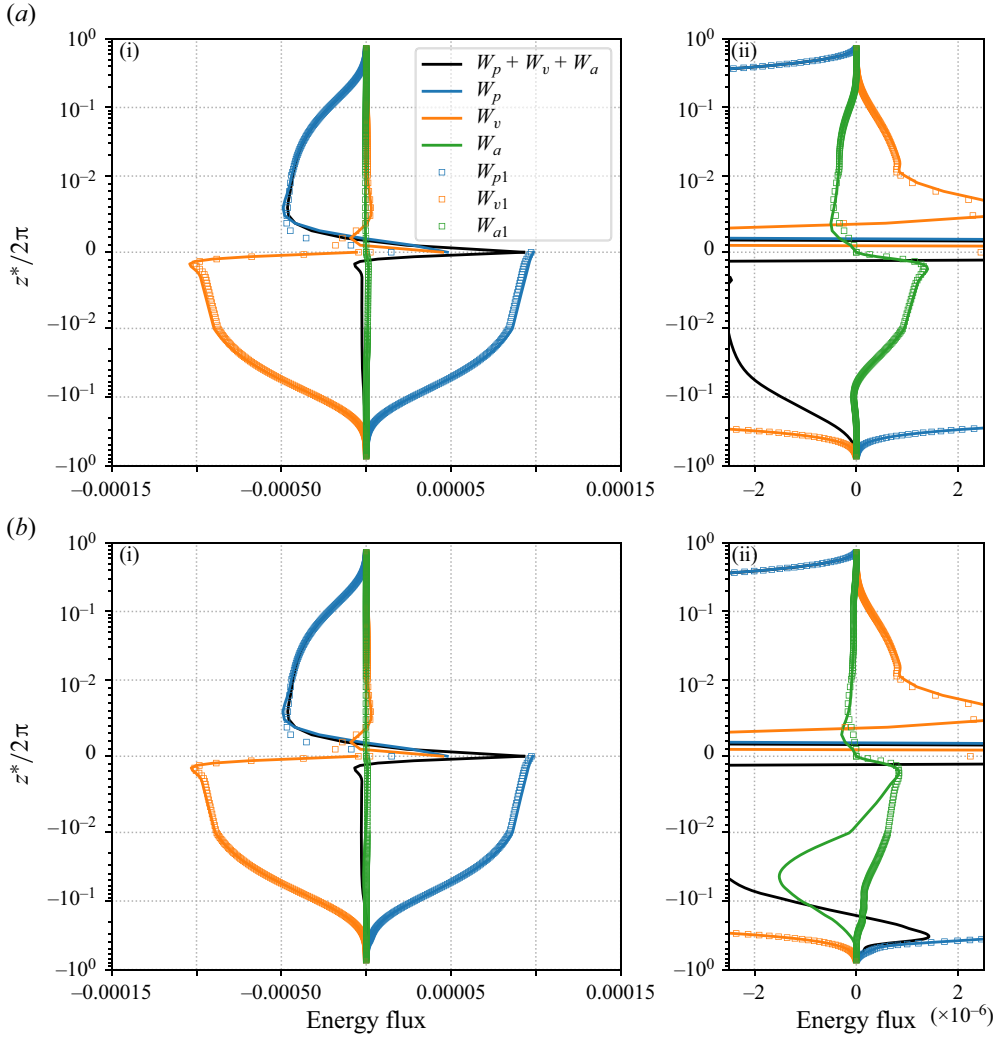
Figure 13. Vertical profiles of the energy flux components defined in (4.10): (*a*,*b*) profiles of the AW-noturb and AW-ctrl cases, respectively, (*a* ii,*b* ii) the same quantities as in (*a* i,*b* i), but the range of the horizontal axis is magnified. The vertical axis is logarithmic for $|z^*/2\pi| \geq 10^{-2}$ and linear for $|z^*/2\pi| < 10^{-2}$.

towards the interface. All of these flux terms are mostly explained with the first-harmonic contributions defined as follows:

$$W_{p1} = 2\mathrm{Re}\left[\hat{\tilde{p}}_{10}\hat{w}_{10}^{\star}\right], \tag{4.16a}$$

$$W_{v1} = -2\rho\mathrm{Re}\left[\hat{u}_{10}\hat{T}_{10}^{xz\star}\right], \tag{4.16b}$$

$$W_{a1} = 2\mathrm{Re}\left[\hat{\omega}_{10}\hat{E}_{10}^{\star}\right]. \tag{4.16c}$$

The KE budget equation terms for the AW-ctrl case are shown in figures 12(*b*) and 13(*b*). Unlike horizontal momentum, the KE budget profile of the AW-ctrl case is very similar to the AW-noturb case and is mostly explained with the first harmonic contributions.

999 A97-30

Therefore, the major energetics of the attenuating interfacial waves of $\lambda \approx 1\,\mathrm{m}$ is dominated by the laminar wave dynamics, even in the presence of wave-induced turbulence. Nevertheless, some differences can be seen in the advective flux in the water side. Although the first harmonic W_{a1} still carries KE upwards, the contributions from other components carry KE downwards, resulting in $W_{a1} < 0$ in the bulk of the water.

4.4. *Comparison of TKE*

In order to illustrate the role of the air–water coupling in turbulence production and to investigate its reproducibility with the wave-averaged framework, two additional simulations were conducted. The new simulations, named AW-CL and W-CL, are replications of the AW-ctrl and W-ctrl cases using the CL equation and virtual wave stress as the boundary condition. We focus on the turbulence in the water side, so they were conducted in the rigid-lid water-side domain $-H_o \leq z \leq 0$, $\eta = 0$. The CL vortex force term with the prescribed Stokes drift $(u^{St}(z, t), 0, 0)$ was added to the governing equation:

$$\frac{\partial u}{\partial t} + u\frac{\partial u}{\partial x} + v\frac{\partial u}{\partial y} + w\frac{\partial u}{\partial z} = -\frac{\partial p}{\partial x} + \frac{1}{Re_o}\left(\frac{\partial^2 u}{\partial x^2} + \frac{\partial^2 u}{\partial y^2} + \frac{\partial^2 u}{\partial z^2}\right), \tag{4.17a}$$

$$\frac{\partial v}{\partial t} + u\frac{\partial v}{\partial x} + v\frac{\partial v}{\partial y} + w\frac{\partial v}{\partial z} = -\frac{\partial p}{\partial y} + \frac{1}{Re_o}\left(\frac{\partial^2 v}{\partial x^2} + \frac{\partial^2 v}{\partial y^2} + \frac{\partial^2 v}{\partial z^2}\right) - u^{St}\left(\frac{\partial v}{\partial x} - \frac{\partial u}{\partial y}\right), \tag{4.17b}$$

$$\frac{\partial w}{\partial t} + u\frac{\partial w}{\partial x} + v\frac{\partial w}{\partial y} + w\frac{\partial w}{\partial z} = -\frac{\partial p}{\partial z} + \frac{1}{Re_o}\left(\frac{\partial^2 w}{\partial x^2} + \frac{\partial^2 w}{\partial y^2} + \frac{\partial^2 w}{\partial z^2}\right) + u^{St}\left(\frac{\partial u}{\partial z} - \frac{\partial w}{\partial x}\right). \tag{4.17c}$$

Here, p is the generalised pressure that includes both the non-hydrostatic pressure and the Bernoulli head effect and was calculated to retain incompressibility. The horizontal and bottom boundary conditions are the same as the wave-resolving simulations. The dynamical boundary condition at $z = 0$ is the prescribed virtual wave stress ((1.2) and (1.4)):

$$\left.\frac{1}{Re_o}\frac{\partial u}{\partial z}\right|_{z=0} = \begin{cases} \tau_{ao}^{vws}(t) & \text{(AW-CL)}, \\ \tau_o^{vws}(t) & \text{(W-CL)}, \end{cases} \qquad \left.\frac{1}{Re_o}\frac{\partial v}{\partial z}\right|_{z=0} = 0. \tag{4.18}$$

Here, the temporal dependence of virtual wave stress is allowed to reflect the attenuating wave amplitude $a(t)$. The vertical structure of the Stokes drift is provided with the linear surface wave solution:

$$u^{St}(z, t) = \frac{[a(t)]^2}{2\sinh^2 H_o}\cosh 2(z + H_o). \tag{4.19}$$

The temporal decay rate of amplitude is provided with the linear theory ((1.1) and (1.3)):

$$a(t) = \begin{cases} a(0)\mathrm{e}^{-\gamma_{ao}t} & \text{(AW-CL)}, \\ a(0)\mathrm{e}^{-\gamma_o t} & \text{(W-CL)}. \end{cases} \tag{4.20}$$

The initial wave amplitude is $a(0) = 0.1$. The simulation was started using the same Gaussian noise as added in the AW-ctrl and W-ctrl cases, and the simulation is conducted until $t = 1200\pi$ with $\Delta t = 2\pi/60$. Overall, the flow field obtained in the wave-averaged cases resembled the wave-filtered field of the corresponding wave-resolving cases.
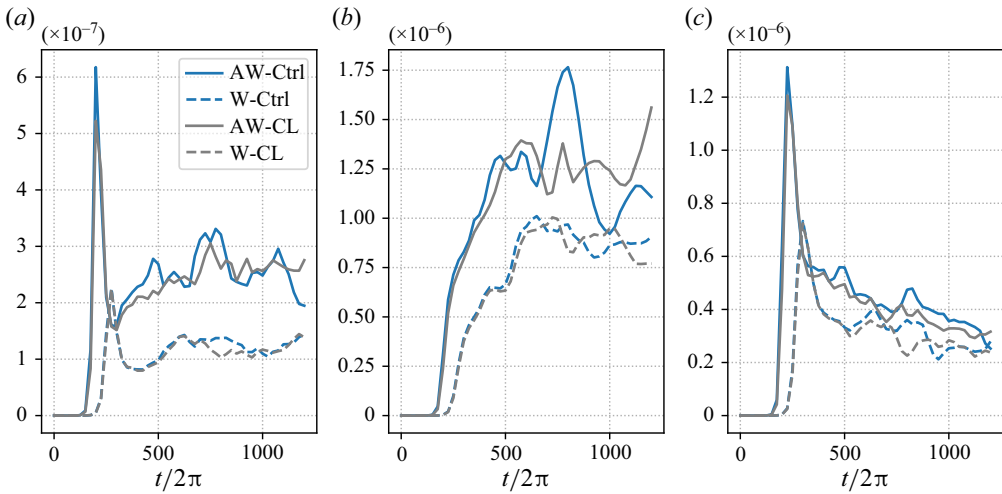
Figure 14. Temporal evolution of the water-side velocity variance, (a) $\overline{u'^2}$, (b) $\overline{v'^2}$, (c) and $\overline{w'^2}$, averaged over $-0.4 \leq z^* \leq 0$ of the AW-ctrl, W-ctrl, AW-CL and W-CL cases. Solid lines show the AW-ctrl and AW-CL cases and dashed lines show the W-ctrl and W-CL cases. Blue lines show wave-resolving simulation results, and the grey lines show wave-averaged simulation results.

To quantitatively compare the temporal growth of the flow field, the variance of the turbulent velocity u', v', w' is examined in the following.

Figure 14 shows the temporal evolution of $\overline{u'^2}$, $\overline{v'^2}$ and $\overline{w'^2}$, averaged over $-0.4 \leq z^* \leq 0$. Each case shows the accelerating growth of variances over $0 \leq t \leq 300$, suggesting some instability mechanism at work. The comparison of the AW-ctrl and W-ctrl cases illustrates that the presence of a coupled air layer intensifies the wave-induced water turbulence. The velocity variance in the initial growth stage of the AW-ctrl and W-ctrl cases clearly differ: the variance grows quicker and reaches a greater value in AW-ctrl. This is consistent with the fact that a stronger Eulerian mean drift was seen in the air–water coupled case than in the water-only case (figure 7). Once the initial instability saturates at $t/2\pi \approx 500$, the time series exhibits more chaotic behaviour. Thereafter, each variance component of AW-ctrl is clearly greater than the corresponding value in W-ctrl.

Comparison between the wave-averaged cases and their corresponding wave-resolving cases illustrates the reproducibility of the simulated wave-induced turbulence in the wave-averaged dynamics. In the initial growth phase ($0 \leq t/2\pi \leq 300$), the wave-averaged cases very well trace the corresponding wave-resolving cases. After the saturated phase ($t/2\pi \approx 500$), the wave-averaged cases show deviation from the wave-resolving cases due to the chaotic behaviour of the mature flow. However, the spread of the time series of the AW-ctrl/CL pair overlaps each other and is distinct from the W-ctrl/CL pair, which is especially visible in the time series of $\overline{u'^2}$. Therefore, we conclude that the simulated wave-induced turbulence can be successfully reproduced using the CL equation and the virtual wave stress as the imposed boundary condition.

5. Discussion and conclusion

To clarify the role of air–water coupling in WL turbulence production, a wave-resolving DNS of the air–water interfacial wave has been conducted and compared with other simulation set-ups such as a free surface wave-resolving DNS. At the bottom of the air, a very sharp SBL develops, where a significant amount of KE is dissipated. As a result,

999 A97-32

the wave attenuation rate is enhanced compared with the water-only case. Even in the presence of WL turbulence, the attenuation rate was well-predicted by the linear theory of Dore (1978).

The simulation results suggest that the WL turbulence is produced by the CL2 instability mechanism under the Eulerian mean drift induced by the horizontal momentum supplied from the attenuated wave. This conclusion qualitatively aligns with the preceding studies, such as Tsai *et al.* (2017) and Fujiwara *et al.* (2020), but the resulting turbulence was intensified due to the enhanced momentum transfer from the wave. The momentum and energy budget analysis revealed the detailed flow of these quantities: although a significant fraction of energy lost from the water is transferred to the air and dissipated there, the momentum of wave motion is confined within the water. The present understanding is crucial for quantitatively interpreting laboratory results and extrapolating them to the field scale, as the water surface is constantly in contact with air in reality.

Among many cases conducted in the tank experiments of Savelyev *et al.* (2012), there are a series of cases with $k = 6.32 \, \mathrm{m}^{-1}$ ($\lambda = 0.99 \, \mathrm{m}$), which is close to the parameter choice of the present simulations ($\lambda \approx 1 \, \mathrm{m}$). The experimental spanwise wavenumber l is evaluated as in Tsai *et al.* (2017), $l = \lambda/L_{eddy}$, where λ is wavelength and L_{eddy} is the eddy size provided in Savelyev *et al.* (2012). Here L_{eddy} was measured at the initial stage of vortex formation, so l is compared with the maximum value of l_s (figure 9), which reflects the characteristic scale of growing instability. In the AW-ctrl and W-ctrl cases ($ak = 0.1$), we obtained $l_s = 15$ and 14, respectively. In Savelyev *et al.* (2012), the case with $ak = 0.136$ led to $l = 13.1$. Although it would be safe to say that the laboratory and numerical experiments roughly agree, the interpretation of the values provided is not so straightforward because of the difference in experiment parameters and evaluation methods.

In the linear stability analysis conducted by Tsai *et al.* (2017), the only non-dimensional number characterising the problem was the Langmuir number

$$\mathrm{La} = \frac{v_o^{3/2}}{a\sigma^{1/2}k^{-1}u_*}, \tag{5.1}$$

where $u_* = (\tau^{vws}/\rho_o)^{1/2}$ is the water-side friction velocity associated with virtual wave stress. They used the water-side only virtual wave stress ($\tau^{vws} = \tau_o^{vws}$) and obtained $\mathrm{La} = v_o/2^{1/2}a^2\sigma$. However, when interpreting the laboratory experiment result, the virtual wave stress based on the theory of Dore (1978, i.e. $\tau^{vws} = \tau_{ao}^{vws}$) would be more appropriate. As a result,

$$\mathrm{La} = \frac{v_o}{2^{1/2}a^2\sigma} \left[1 + \frac{\rho_a}{\rho_o} \frac{Re_o}{(2Re_a)^{1/2}} \right]^{-1/2} \tag{5.2}$$

is obtained. Assuming the material parameters at $10\,^\circ\mathrm{C}$ (§ 1) and wavelength $\lambda = 140 \, \mathrm{cm}$, the Langmuir number is reduced by 36 % compared with the water-only case, and the reduction is greater for longer waves. This modification of the Langmuir number somewhat reduces the scatter of the experimental data by Savelyev *et al.* (2012) shown in figure 9 of Tsai *et al.* (2017). When the Langmuir number is evaluated as (5.1), the correlation coefficient between $-\log_{10}(\mathrm{La})$ and l is 0.45, and when (5.2) is used instead, it increases to 0.51.

Consequently, a physically plausible approach to synthesise the parameterisations for LCs and WL turbulence is to use the wave-averaged large-eddy simulation based on the CL equation with the surface wind stress incremented by the virtual wave stress. Many of the present parameterisations that incorporate mixing by LCs are based on this framework

without virtual wave stress and employ the friction velocity $u_* \equiv (\tau/\rho_o)^{1/2}$ to characterise the shear of the Eulerian current (e.g. Li *et al.* 2019). Therefore, the effect of virtual wave stress can be easily incorporated into these parameterisations by increasing u_*^2 by τ_{ao}^{vws}/ρ_o.

For the estimation of virtual wave stress under a realistic wind-wave spectrum, more understanding of the energy dissipation mechanism is required. One important issue remaining to be solved is the turbulence transition of the air-side Stokes layer. One of the state-of-the-art wave model source function packages (Ardhuin *et al.* 2010) assumes that such a transition occurs when the air-side significant Reynolds number $2u_{orb,s}H_s/\nu_a$, where $u_{orb,s}$ is the significant surface orbital velocity and H_s is the significant wave height, exceeds a certain limit value. Once the turbulence transition occurs, wave energy will be dissipated more efficiently, and the virtual wave stress will be further increased. In our wave-resolving DNS, such a transition could not be observed due to the smallness of the Reynolds number, so a further experimental or computational investigation of this boundary layer under a higher Reynolds number is necessary. Even without turbulence transition, the large-amplitude waves can trigger other effects, such as the generation of parasitic capillary waves and microbreaking (e.g. Tsai & Hung 2007; Deike, Popinet & Melville 2015), modulational instability interacting with currents Li & Chabchoub (2024) and so on. Such finite-amplitude effects should be explored further in the future. If the linear laminar theory of Dore (1978) remains applicable and the deep-water dispersion relation is assumed, the virtual wave stress can be estimated from a wave variance density spectrum $E(\sigma, \theta)$ following

$$(\tau_x^{vws}, \tau_y^{vws}) = \iint G(\sigma)E(\sigma, \theta)(\cos\theta, \sin\theta)\, \mathrm{d}\theta\, \mathrm{d}\sigma, \qquad (5.3)$$

where the virtual wave stress transfer function $G(\sigma)$ is defined as follows:

$$G(\sigma) = 2\sigma^2 \left[\frac{2}{Re_o}\rho_o + \left(\frac{2}{Re_a}\right)^{1/2}\rho_a \right] = \frac{4\rho_o\nu_o}{g^2}\sigma^5 + \frac{2\sqrt{2}\rho_a\nu_a^{1/2}}{g}\sigma^{7/2}. \qquad (5.4)$$

For reference, with the physical parameters at $10\,°\mathrm{C}$, $G(\sigma)$ is 1.4×10^0, 7.0×10^{-3} and 9.5×10^{-4} N m^{-4} for 1-, 4- and 7-second-period waves, respectively. With a 7-second-period swell with one-side amplitude of 1 m, virtual wave stress would be $4.75 \times 10^{-4}\,\mathrm{N\,m^{-2}}$. Therefore, the influence of additional momentum flux via virtual wave stress is well below a typical wind stress value unless the turbulence transition occurs. Nevertheless, its effect is worth exploring in the future because the CL2 instability efficiently produces near-surface turbulence even under slack conditions, potentially influencing phenomena such as the sea-surface skin temperature.

999 A97-34

Author ORCID.

Yasushi Fujiwara https://orcid.org/0000-0003-2797-2072.

Appendix A. Performance test of the two-phase model

A.1. *Small- and finite-amplitude interfacial waves*

First, let us consider the inviscid interfacial waves of small amplitude to study the model reproducibility of dispersion relation and its resolution dependence. The dispersion relation of small-amplitude deep-water interfacial gravity waves is given by

$$\sigma = \sqrt{\frac{\rho_o - \rho_a}{\rho_o + \rho_a} gk}, \tag{A1}$$

where k is the horizontal wave number and σ is the angular frequency of the wave.

We normalised the equation with the length scale k^{-1} and time scale $\sqrt{gk}$. Let us consider a x–z two-dimensional domain with the domain size $(L_x, H_a, H_o) = (2\pi, 4\pi, 4\pi)$ (L_x is the domain size in the x direction). For the interfacial wave with the horizontal wavenumber 1, this depth of domain is effectively the deep-water condition. The number of grid points is 16 in the horizontal. Both the air and water sides were discretised with uniformly distributed N_z grid points in the vertical, and the sensitivity to the vertical resolution was investigated through cases with $N_z = (16, 32, 64, 128, 256)$. Two sets of density, $(\rho_a, \rho_o) = (1, 10)$ and $(1, 1000)$, were considered in each N_z. The simulation was initialised using the orbital velocity of propagating small-amplitude interfacial wave:

$$u(x, z, 0) = -a\sigma e^{-z} \cos x, \quad w(x, z, 0) = a\sigma e^{-z} \sin x, \quad \text{(air)}, \tag{A2a}$$

$$u(x, z, 0) = a\sigma e^{z} \cos x, \quad w(x, z, 0) = a\sigma e^{z} \sin x, \quad \text{(water)}. \tag{A2b}$$

Here, $a = 10^{-4}$ was chosen, and σ was provided with (A1). The simulation was conducted with $\Delta t = 2\pi/100$ for over 120 periods, and the wave period was calculated as the average of the first 100 waves obtained from the zero-up-cross analysis.

The angular frequency calculated from the simulation is plotted against N_z in figure 15(a). With sufficient vertical resolution, the model can accurately simulate the dispersion relation of the deep-water interfacial waves. The error is dominated by the vertical discretisation in this setting and is of $O(\Delta z^{*2})$. The relative error is 0.06 % with $N_z = 128$ ($\Delta z^* = 2\pi/64$).

We also examined the error in total energy

$$E(t) = \frac{\rho_a}{2} \iint_{air} (u^2 + w^2) \, dx \, dz + \frac{\rho_o}{2} \iint_{water} (u^2 + w^2) \, dx \, dz + \frac{(\rho_o - \rho_a)g}{2} \int \eta^2 \, dx, \tag{A3}$$

which should ideally be conserved. The numerical energy amplification rate γ was evaluated by fitting $E(t) = E_0 e^{\gamma t}$. In cases where $\rho_o = 1000$, $\gamma \approx -1.1 \times 10^{-6}$ regardless of N_z. This artificial attenuation is dominated by the temporal discretisation of $O(\Delta t^5)$, as it is reduced to $\gamma \approx -3.3 \times 10^{-8}$ with halved timestep. Since the mass and momentum equations are discretised based on the flux form (2.8) and (2.9), the error in mass and momentum was extremely small, with relative error below $O(10^{-12})$ even for the finite-amplitude cases described in the following.
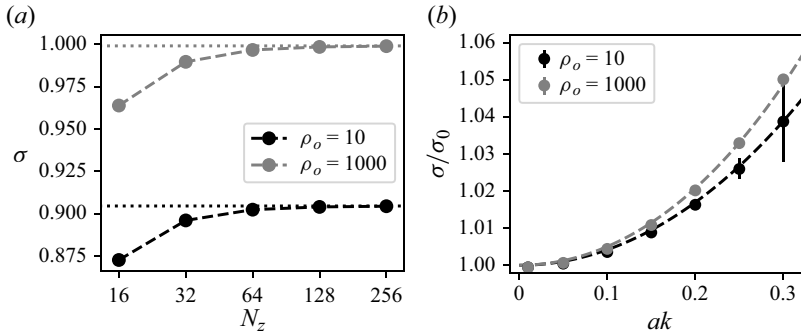
Figure 15. (*a*) Angular frequency and (*b*) numerical energy decay rate of simulated interfacial waves with different density ratios and vertical resolution. Horizontal dotted lines in (*a*) denote the linear dispersion relation of respective density ratios. Dashed lines in (*b*) denote the asymptotic dispersion relation derived by Tsuji & Nagata (1973).

Next, we considered the dispersion relation of finite-amplitude waves to examine the model performance on weakly nonlinear phenomena. As in free-surface waves (Stokes 1847), nonlinearity modifies the dispersion relation of the interfacial gravity waves. Tsuji & Nagata (1973) applied the Stokes expansion to the deep-water interfacial wave problem and obtained the asymptotic solution to the fifth order in interfacial slope *ak*. Following Tsuji & Nagata (1973), the angular frequency is

$$\sigma = \sigma_0 \left[1 + \frac{1}{2} \frac{\rho_o{}^2 + \rho_a{}^2}{(\rho_o + \rho_a)^2} (ak)^2 + \frac{(\rho_o - \rho_a)^2 (5\rho_o^2 - 14\rho_o\rho_a + 5\rho_a^2)}{4(\rho_o + \rho_a)^4} (ak)^4 \right] \quad \text{(A4)}$$

to the fifth order in *ak*. Here, $\sigma_0 = [gk(\rho_o - \rho_a)/(\rho_o + \rho_a)]^{1/2}$ is the angular frequency of the small-amplitude deep-water wave.

We adopted the same normalisation and domain as in the small-amplitude cases. The number of grid points is 64 in horizontal and 128 in vertical in both air and water sides. Two sets of density, $(\rho_a, \rho_o) = (1, 10)$ and $(1, 1000)$, were considered, and the initial interfacial slope was set to $ak = 0.01, 0.05, 0.10, 0.15, 0.20, 0.25$ and 0.30. The fifth-order Stokes wave solution of Tsuji & Nagata (1973) was used as the initial field, and the simulation was conducted with the integration time step of $\Delta t = 2\pi/200$. The zero-up-cross analysis was applied to the interface elevation at a certain point, and the wave periods of the first 50 waves were analysed.

The simulated angular frequency normalised with the linear angular frequency σ_0 in each density ratio is plotted against *ak* in figure 15(*b*). The average of the angular frequencies of the 50 waves is denoted with circles, and their standard deviation is denoted with error bars. The averaged angular frequencies follow the asymptotic dispersion relation well within the cases we studied. However, in large-amplitude cases ($ak = 0.25, 0.30$) of $\rho_o = 10$, the initial wave shape was not retained and the wave periods showed some scatter. In general, increased interfacial slopes lead to an increased number of iterations required for solving the Poisson equation. In $\rho_o = 1000$ series, the number of iterations required for convergence was 7 with $ak = 0.10$ but 15 with $ak = 0.30$.

A.2. *Laminar Miles instability*

Subsequently, we studied the wind–wave interaction problem. We adopted the problem set-up introduced by Miles (1957), where a parallel shear flow interacts with the underlying

small-amplitude surface waves via interfacial pressure. Here, inviscid laminar flow was considered following the simplification made by Miles (1957). Logarithmic wind profiles are superposed over small-amplitude gravity wave as the initial condition. The growth rate of the waves evaluated over the first tens of wave periods of the simulations, which corresponds to the linear instability phase, and is compared with the analytic growth rate of Miles (1959).

Let us consider inviscid air and water with a density ratio of $\rho_o/\rho_a = 1.0 \times 10^3$. There, a small-amplitude interfacial deep-water wave with a horizontal wavenumber k will have angular frequency $\sigma = [gk(\rho_o - \rho_a)/(\rho_o + \rho_a)]^{1/2}$. We used k^{-1} and σ^{-1} to normalise the length and time scales, respectively. A x–z two-dimensional domain with domain size $(L_x, H_a, H_o) = (2\pi, 2\pi, 2\pi)$ was considered. The domain was discretised with 12 grid points in the horizontal. The vertical grid points clustered near the interface, with layer thickness varying exponentially at a ratio of 1.02. We investigated the sensitivity to the vertical resolution, which is detailed in the following.

Let us consider a logarithmic wind profile $u = (u_*/\kappa) \log(z/z_0)$ in the air side, as employed in the calculation of growth rate by Miles (1959). Here, u_* is the friction velocity, $\kappa = 0.4$ is von Kármán constant and the roughness length z_0 was specified using the non-dimensionalised Charnock's relation $z_0 = 0.01u_*^2$. With this, the critical level z_c can be related to u_* as $z_c = 0.01u_*^2 e^{\kappa/u_*}$, where z_c is the height at which $u(z_c) = 1$. Four critical levels $z_c = 2\pi/10, 2\pi/40, 2\pi/160$ and $2\pi/640$ were considered. For each z_c, the first vertical layer thickness was adjusted such that the layer between the critical level and the interface would be resolved with $N_c = 2, 4, 8$ and 16 grid points. The total vertical grid points in the air side varied from 17 ($z_c = 2\pi/10, N_c = 2$) to 269 ($z_c = 2\pi/640, N_c = 16$). The water-side layer thicknesses were set symmetrically to the air side.

As an initial condition, the air-side logarithmic wind profile is superposed on the small-amplitude orbital motion (A2) with $a = 10^{-4}$. Simulation is conducted for 100π with $\Delta t = 2\pi/360$. Following Miles (1957), the wave growth rate was evaluated as $\beta = \text{Im}(\hat{\tilde{p}}/\hat{\eta})/(\rho_a u_*^2/\kappa^2)$, where hat denotes the Fourier coefficient of the component with horizontal wavenumber $k = 1$ and Im denotes the imaginary part. We evaluated β as the time average over $2\pi \leq t \leq 62\pi$.

The temporal evolution of wave amplitude for a case with $kz_c = 2\pi/640$ is shown in figure 16. The amplitude is evaluated as $a(t) = 2|\hat{\eta}|$. Initially, the waves in all cases grow at the same rate. Over the simulation period we have conducted, we cannot clearly distinguish linear and exponential growth, but we refer to it as linear growth for convenience. Cases with lower vertical resolution start to deviate from the linear growth at a certain point. The wave of the $N_c = 16$ case remains in the linear growth phase throughout the simulation period, which is about 50 wave periods. When the lower-resolution cases deviate from the linear growth, the flow structure near the critical level seems to be no longer maintained in phase with the wave because of the coarse representation of the wind profile.

The evaluated wave growth rate β was plotted against the critical level normalised with the wavenumber in figure 17 together with the theoretical curve computed by Miles (1959). With sufficient vertical resolution like $N_c = 8$ or 16, our simulation effectively reproduces the theoretical growth rate. This suggests that the model can accurately reproduce the weak coupling of sheared wind and water waves, a crucial process in wind–wave interaction.

Appendix B. Modification of model formulation for the air-side-only simulations

The numerical procedure for the two-phase fluid can be extended to the air-side-only simulation where $\eta(x, y, t)$ is provided externally. In this case, the unknown variables are
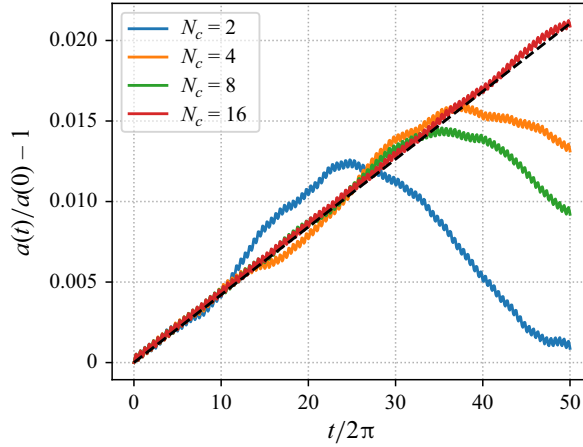
Figure 16. Time evolution of wave amplitude $a(t) = 2|\hat{\eta}|$ for cases with $z_c = 2\pi/640$ and $N_c = 2$, 4, 8 and 16. The black dashed line shows the growth following the amplitude growth rate $\zeta_a = (1/2)(\rho_a/\rho_o)(u_*/\kappa c)^2 \beta$, where the normalised growth rate β is obtained from the case with $z_c = 2\pi/640$ and $N_c = 16$. The evaluation of β in figure 17 was conducted over $2\pi \leq t \leq 62\pi$.
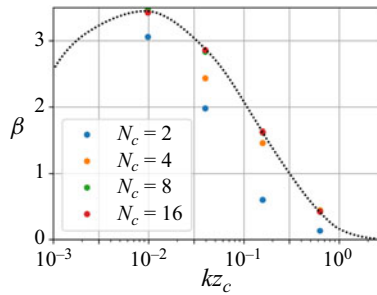

Figure 17. Dependence of growth rate β on z_c and the number of grid points below the critical level N_c. The dotted line shows the analytic solution by Miles (1959), traced from its figure 2.

U, V and W (K_a points in vertical), and P in the air-side domain and the interface ($K_a + 1$ points in vertical). The kinematic boundary condition at the interface is shown in (2.3), whose left-hand side is a known function. Time advancement of U, V and W is conducted with (2.8a–c). The pressure Poisson equation at the air-side layer centres ($k = 1, \ldots, K_a$) is shown in (2.13). At the air–water interface ($k = 0$), (2.15) is modified based on the kinematic boundary condition (2.3) for $z = \eta + 0$:

$$\left(-\frac{1}{h_a^2} \frac{\partial P}{\partial z^*} + \frac{G^z}{h_a} \right)_{1/2} - \frac{\eta_{x*}}{h_a} \left[-\frac{\partial P}{\partial x^*} + \left(\frac{z_{x*}P}{h_a} \right)_{z^*} + G^x \right]_1 - \frac{\eta_{y*}}{h_a} \left[-\frac{\partial P}{\partial y^*} + \left(\frac{z_{y*}P}{h_a} \right)_{z^*} + G^y \right]_1$$
$$+ \left(\frac{1}{h_a} \right)_{t^*} W_{1/2} - \left(\frac{\eta_{x*}}{h_a} \right)_{t^*} U_1 - \left(\frac{\eta_{y*}}{h_a} \right)_{t^*} V_1 = \frac{\partial^2 \eta}{\partial t^{*2}}. \quad \text{(B1)}$$

Since we did not need to match the definition of P in the air- and water-side domains, we simply define P_0 as $P_0 \equiv p$, and the vertical derivatives in (B1) is interpreted accordingly.

999 A97-38
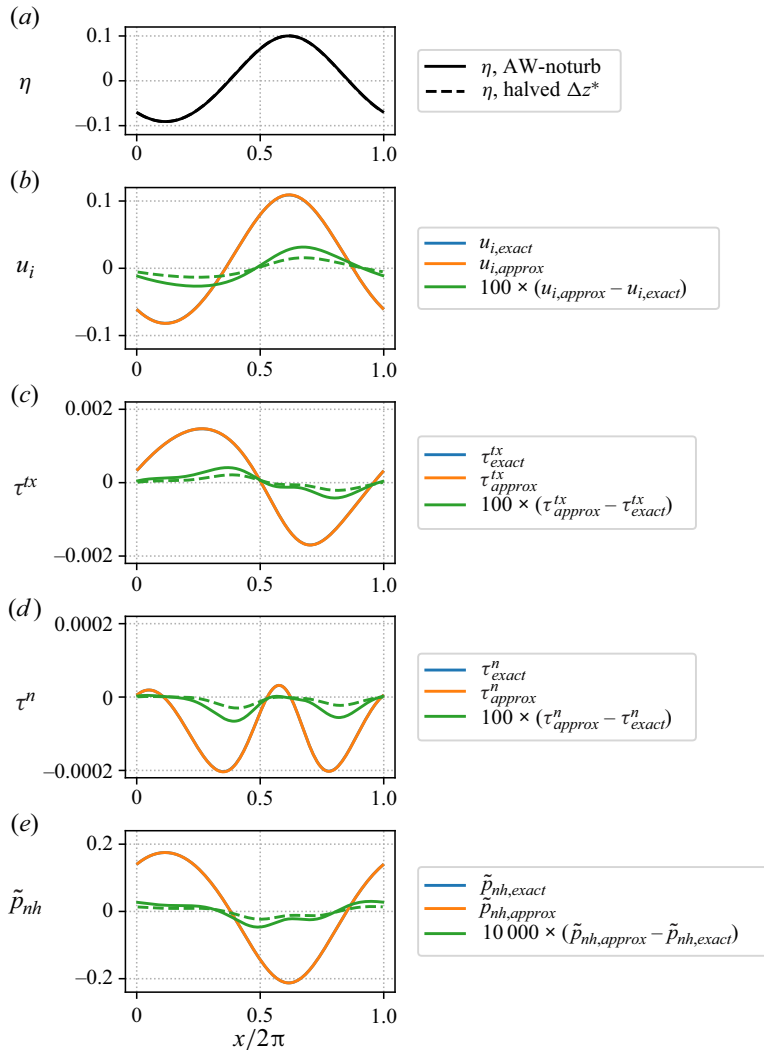
Figure 18. Instantaneous distribution of (*a*) η, (*b*) u_i, (*c*) τ_i^{tx}, (*d*) air-side τ_i^n and (*e*) air-side $\tilde{p}_{nh}$ diagnosed at $t/2\pi = 300.08$ of the AW-noturb and AW-noturb-highres cases. In panels (*b*–*e*), the exact (subscript '*exact*', obtained through iteration) and the approximated (subscript '*approx*', obtained through approximation introduced in §2.3) distributions and the difference between them are shown. Blue (exact) and orange (approximated) curves nearly overlap. Dashed lines show (*a*) η and (*b*–*e*) difference between exact and approximated quantities in the AW-noturb-highres case, and the solid and dashed lines are overlapped in (*a*).

Appendix C. Evaluation of error induced by interfacial velocity approximation

In the present model, the interfacial velocity to evaluate the viscous stress is approximated with the value at the water-side top layer to reduce computational cost. As a result, the interfacial velocity is expected to contain error of $O(\rho_a \nu_a / \rho_o \nu_o)$ as discussed in §2.3. Here, the influence of the error introduced by the approximation is discussed by evaluating the 'exact' interfacial velocity. From the instantaneous velocity fields (every 50π time interval) of the AW-noturb case, the exact interfacial velocity u_i is obtained through the iterative method such that the viscous stress evaluated with the air- and water-side velocity gradients would satisfy the continuity of the tangential and normal stresses. The iteration
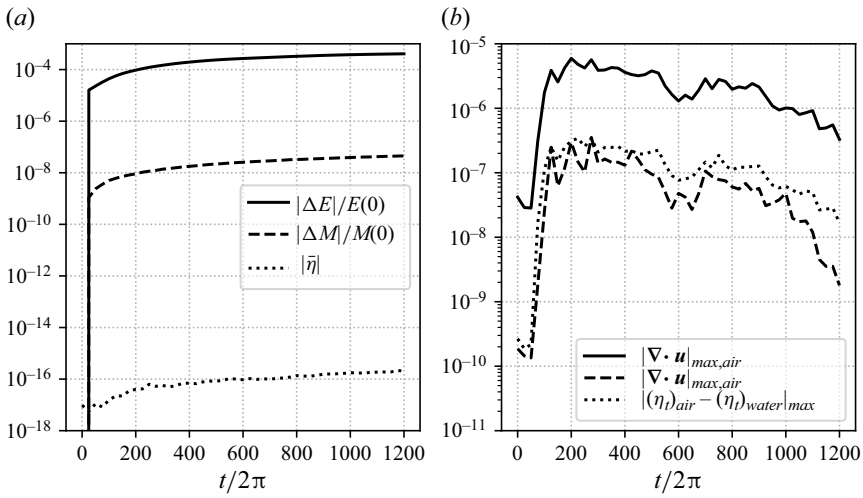
999 A97-39

Figure 19. Time series of numerical error in the AW-a2 case: (*a*) error in total mass, horizontal momentum and energy, as defined in the text; and (*b*) maximum velocity divergence and mass discontinuity at the interface.
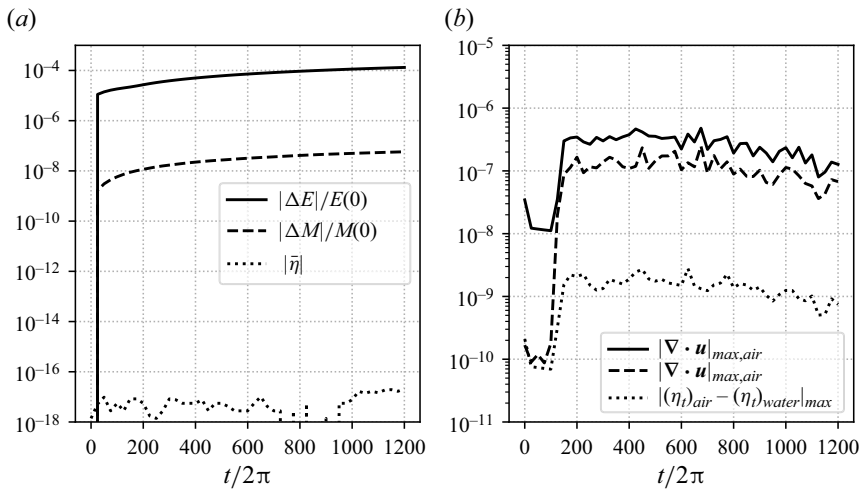

Figure 20. Same as figure 19, but for the AW-deepnoise case.

was conducted by alternately updating the interfacial velocity and stress until convergence. We have evaluated the error in the AW-ctrl as well, and it was almost identical to the AW-noturb case. Therefore, to facilitate the sensitivity analysis conducted later, we focus on the AW-noturb case here.

In figure 18, the interfacial velocity u_i and the interfacial stress components τ_i^{tx}, τ_i^n and $\tilde{p}_{nh}$ with exact and approximated formulations are shown for the AW-noturb case at $t/2\pi = 300.08$. The following descriptions apply for other times in the simulation period. As expected from the theoretical analysis, the interfacial velocity contains the relative error of $O(1)\%$. This results in $O(1)\%$ relative error in viscous stress at the interface. The error in interfacial pressure is $O(0.01)\%$ of the dynamical values, but its absolute error $O(10^{-5})$ is similar to that of τ_i^{tx}. Averaged over the simulation period, the net horizontal momentum transfer from water to air is enhanced by 7.7×10^{-8} in the
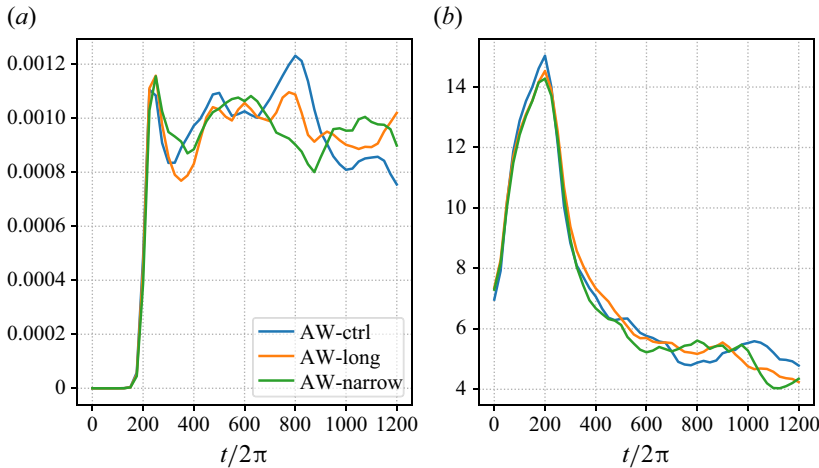
999 A97-40

(*a*)

(*b*)

Figure 21. Time series of (*a*) TKE and (*b*) spanwise wavelength l_s, averaged over $-0.4 \leq z^* \leq 0$.

approximated formulation compared with the exact evaluation. This amount of error is $O(0.1)\%$ of the momentum flux controlling the major dynamics (figure 11). In addition, the net energy flux from water to air is reduced by 9.8×10^{-7} in the approximated formulation, which is $O(1)\%$ of the major energy flux (figure 13). Therefore, the influence of the interfacial velocity approximation on the dynamics reported in § 4 can be considered minor.

To examine the sensitivity to the vertical resolution, an additional case with doubled vertical resolution (AW-noturb-highres) is conducted. There, the numbers of vertical grid points are doubled in both air and water sides, and the thicknesses of layer neighbouring the interface is specified to be $0.25(2/Re_{a,o})^{1/2}$ (half of the AW-noturb case). As a result, the vertical grid spacings are halved compared with the AW-noturb case almost uniformly throughout the domain. The interfacial velocity and stress errors are shown as green dashed lines in figure 18(*b–e*). The magnitude of the error is nearly halved compared with the AW-noturb case, so the error introduced by this approximation is proportional to Δz^*.

Appendix D. Error time series of the AW-a2 and AW-deepnoise cases

The numerical error is monitored for the AW-a2 and AW-deepnoise cases and shown in figures 19 and 20, respectively. In the AW-a2 case, the numerical error is greater than cases with $ak = 0.1$ (figures 2 and 20), but it is still much smaller than the signals from major dynamics. For example, the numerical error of total energy led to increase of 0.04 % compared with $E(0)$ over 1000 wave periods, but it is 0.1 % of the energy dissipation induced by viscosity. In addition, mass divergence $|\nabla \cdot \boldsymbol{u}|$ is greater than AW-ctrl, but is still about 10^{-5} smaller than the characteristic strain rate by the wave orbital motion ($ak\sigma = 0.2$).

Appendix E. Sensitivity of turbulence structure to domain size

The periodic boundary conditions could restrict the turbulent structure to certain wavenumbers and affect the results. To examine the possible domain dependence of the result, we consider two sensitivity tests with a domain size modified from the

AW-ctrl, AW-narrow ($L_x = 2\pi$, $L_y = 1.8\pi$) and AW-long ($L_x = 4\pi$, $L_y = 1.8\pi$) cases. Sensitivity to spanwise (streamwise) domain size can be studied by comparing the AW-ctrl and AW-narrow (AW-long and AW-narrow) cases. In figure 21, the temporal evolution of waterside TKE and spanwise wavelength l_s averaged over $-0.4 \leq z^* \leq 0$ are shown. Both TKE and l_s agree among cases in general. There are some time-dependent fluctuations after the turbulence becomes mature, but there is no clear bias in any of the three. Therefore, the general water-side turbulence behaviour of the AW-ctrl case can be considered independent of the domain size.

On the other hand, the domain size independence on the air side is difficult to ensure due to the large vortex structure. In both the AW-ctrl and AW-narrow cases, the number of major vortex pairs in the air side was two, which means that the major spanwise wavenumber l_s is different. However, the vortices in the air do not play a major role in the dynamics of wave attenuation, the dynamical understanding obtained in the AW-ctrl case remains unchanged.

REFERENCES

ARDHUIN, F., *et al.* 2010 Semiempirical dissipation source functions for ocean waves. Part I. Definition, calibration, and validation. *J. Phys. Oceanogr.* **40** (9), 1917–1941.

BABANIN, A.V. 2006 On a wave-induced turbulence and a wave-mixed upper ocean layer. *Geophys. Res. Lett.* **33**, L20605.

BABANIN, A.V. & HAUS, B.K. 2009 On the existence of water turbulence induced by nonbreaking surface waves. *J. Phys. Oceanogr.* **39** (10), 2675–2679.

BELCHER, S.E., *et al.* 2012 A global perspective on Langmuir turbulence in the ocean surface boundary layer. *Geophys. Res. Lett.* **39**, L18605.

CAO, T. & SHEN, L. 2021 A numerical and theoretical study of wind over fast-propagating water waves. *J. Fluid Mech.* **919**, A38.

COLAGROSSI, A. & LANDRINI, M. 2003 Numerical simulation of interfacial flows by smoothed particle hydrodynamics. *J. Comput. Phys.* **191** (2), 448–475.

CRAIK, A.D.D. & LEIBOVICH, S. 1976 A rational model for Langmuir circulations. *J. Fluid Mech.* **73** (03), 401–426.

D'ASARO, E.A. 2014 Turbulence in the upper-ocean mixed layer. *Ann. Rev. Mar. Sci.* **6**, 101–115.

DAI, D., QIAO, F., SULISZ, W., HAN, L. & BABANIN, A. 2010 An experiment on the nonbreaking surface-wave-induced vertical mixing. *J. Phys. Oceanogr.* **40** (9), 2180–2188.

DEIKE, L., POPINET, S. & MELVILLE, W.K. 2015 Capillary effects on wave breaking. *J. Fluid Mech.* **769**, 541–569.

DORE, B.D. 1978 Some effects of the air–water interface on gravity waves. *Geophys. Astrophys. Fluid Dyn.* **10** (1), 215–230.

FENTON, J.D. 1985 A fifth-order Stokes theory for steady waves. *ASCE J. Waterway Port Coastal Ocean Engng* **111** (2), 216–234.

FUJIWARA, Y. & YOSHIKAWA, Y. 2020 Mutual interaction between surface waves and Langmuir circulations observed in wave-resolving numerical simulations. *J. Phys. Oceanogr.* **50** (8), 2323–2339.

FUJIWARA, Y., YOSHIKAWA, Y. & MATSUMURA, Y. 2018 A wave-resolving simulation of Langmuir circulations with a nonhydrostatic free-surface model: comparison with Craik–Leibovich theory and an alternative Eulerian view of the driving mechanism. *J. Phys. Oceanogr.* **48** (8), 1691–1708.

FUJIWARA, Y., YOSHIKAWA, Y. & MATSUMURA, Y. 2020 Wave-resolving simulations of viscous wave attenuation effects on Langmuir circulation. *Ocean Model.* **154**, 101679.

FULGOSI, M., LAKEHAL, D., BANERJEE, S. & DE ANGELIS, V. 2003 Direct numerical simulation of turbulence in a sheared air–water flow with a deformable interface. *J. Fluid Mech.* **482**, 319–345.

GUO, X. & SHEN, L. 2013 Numerical study of the effect of surface waves on turbulence underneath. Part 1. Mean flow and turbulence vorticity. *J. Fluid Mech.* **733**, 558–587.

GUO, X. & SHEN, L. 2014 Numerical study of the effect of surface wave on turbulence underneath. Part 2. Eulerian and Lagrangian properties of turbulence kinetic energy. *J. Fluid Mech.* **744**, 250–272.

HAO, X. & SHEN, L. 2019 Wind–wave coupling study using LES of wind and phase-resolved simulation of nonlinear waves. *J. Fluid Mech.* **874**, 391–425.

HARLOW, F.H. & WELCH, J.E. 1965 Numerical calculation of time-dependent viscous incompressible flow of fluid with free surface. *Phys. Fluids* **8** (12), 2182.

IMAMURA, H., YOSHIKAWA, Y. & FUJIWARA, Y. n.d. Direct numerical simulations of the nonbreaking surface-wave-induced turbulence. *Ocean Dyn.* (submitted).

KOMORI, S., KUROSE, R., IWANO, K., UKAI, T. & SUZUKI, N. 2010 Direct numerical simulation of wind-driven turbulence and scalar transfer at sheared gas–liquid interfaces. *J. Turbul.* **11**, N32.

LAMB, H. 1932 *Hydrodynamics*. The University Press.

LANGMUIR, I. 1938 Surface motion of water induced by wind. *Science* **87** (2250), 119–123.

LEIBOVICH, S. 1983 The form and dynamics of Langmuir circulations. *Annu Rev. Fluid Mech.* **15** (1), 391–427.

LI, Q., *et al.* 2019 Comparing ocean surface boundary vertical mixing schemes including Langmuir turbulence. *J. Adv. Model. Earth Syst.* **11** (11), 3545–3592.

LI, Y. & CHABCHOUB, A. 2024 How currents trigger extreme sea waves, the roles of stokes drift, Eulerian return flow, and a background flow in the open ocean. *Geophys. Res. Lett.* **51** (6), e2023GL107381.

LI, T. & SHEN, L. 2022 The principal stage in wind–wave generation. *J. Fluid Mech.* **934**, A41.

LIN, M.-Y., MOENG, C.-H., TSAI, W.-T., SULLIVAN, P.P. & BELCHER, S.E. 2008 Direct numerical simulation of wind–wave generation processes. *J. Fluid Mech.* **616**, 1–30.

LOMBARDI, P., DE ANGELIS, V. & BANERJEE, S. 1996 Direct numerical simulation of near-interface turbulence in coupled gas–liquid flow. *Phys. Fluids* **8** (6), 1643–1665.

LONGUET-HIGGINS, M.S. 1953 Mass transport in water waves. *Phil. Trans. R. Soc. Lond.* A **245** (903), 535–581.

LONGUET-HIGGINS, M.S. 1969 A nonlinear mechanism for the generation of sea waves. *Proc. R. Soc. Lond.* A **311** (1506), 371–389.

MILES, J.W. 1957 On the generation of surface waves by shear flows. *J. Fluid Mech.* **3** (2), 185–204.

MILES, J.W. 1959 On the generation of surface waves by shear flows. Part 2. *J. Fluid Mech.* **6** (4), 568–582.

PHILLIPS, O.M. 1966 *The Dynamics of the Upper Ocean*. Cambridge University Press.

PLESKACHEVSKY, A., DOBRYNIN, M., BABANIN, A.V., GÜNTHER, H. & STANEV, E. 2011 Turbulent mixing due to surface waves indicated by remote sensing of suspended particulate matter and its implementation into coupled modeling of waves, turbulence, and circulation. *J. Phys. Oceanogr.* **41** (4), 708–724.

POPINET, S. 2003 Gerris: a tree-based adaptive solver for the incompressible Euler equations in complex geometries. *J. Comput. Phys.* **190** (2), 572–600.

SAVELYEV, I.B., MAXEINER, E. & CHALIKOV, D. 2012 Turbulence production by nonbreaking waves: laboratory and numerical simulations. *J. Geophys. Res.: Oceans* **117**, C00J13.

STOKES, G.G. 1847 On the theory of oscillatory waves. *Trans. Camb. Phil. Soc.* **8**, 441–455.

SULLIVAN, P.P., EDSON, J.B., HRISTOV, T. & MCWILLIAMS, J.C. 2008 Large-eddy simulations and observations of atmospheric marine boundary layers above nonequilibrium surface waves. *J. Atmos. Sci.* **65** (4), 1225–1245.

SULLIVAN, P.P. & MCWILLIAMS, J.C. 2010 Dynamics of winds and currents coupled to surface waves. *Annu. Rev. Fluid Mech.* **42**, 19–42.

SULLIVAN, P.P., MCWILLIAMS, J.C. & MOENG, C.-H. 2000 Simulation of turbulent flow over idealized water waves. *J. Fluid Mech.* **404**, 47–85.

SUSSMAN, M., ALMGREN, A.S., BELL, J.B., COLELLA, P., HOWELL, L.H. & WELCOME, M.L. 1999 An adaptive level set approach for incompressible two-phase flows. *J. Comput. Phys.* **148** (1), 81–124.

TEIXEIRA, M.A.C. & BELCHER, S.E. 2002 On the distortion of turbulence by a progressive surface wave. *J. Fluid Mech.* **458**, 229–267.

TSAI, W.-T., CHEN, S.-M. & LU, G.-H. 2015 Numerical evidence of turbulence generated by nonbreaking surface waves. *J. Phys. Oceanogr.* **45** (1), 174–180.

TSAI, W.-T., CHEN, S.-M., LU, G.-H. & GARBE, C.S. 2013 Characteristics of interfacial signatures on a wind-driven gravity-capillary wave. *J. Geophys. Res.: Oceans* **118** (4), 1715–1735.

TSAI, W.-T. & HUNG, L.-P. 2007 Three-dimensional modeling of small-scale processes in the upper boundary layer bounded by a dynamic ocean surface. *J. Geophys. Res.: Oceans* **112**, C02019.

TSAI, W.-T. & LU, G.-H. 2023 A numerical study on Langmuir circulations and coherent vortical structures beneath surface waves. *J. Fluid Mech.* **969**, A30.

TSAI, W.-T., LU, G.-H., CHEN, J.-R., DAI, A. & PHILLIPS, W.R.C. 2017 On the formation of coherent vortices beneath nonbreaking free-propagating surface waves. *J. Phys. Oceanogr.* **47** (3), 533–543.

TSUJI, Y. & NAGATA, Y. 1973 Stokes' expansion of internal deep water waves to the fifth order. *J. Oceanogr. Soc. Japan* **29**, 61–69.

VERON, F. & MELVILLE, W.K. 2001 Experiments on the stability and transition of wind-driven water surfaces. *J. Fluid Mech.* **446**, 25–65.

VILLAS BÔAS, A.B., *et al.* 2019 Integrated observations of global surface winds, currents, and waves: requirements and challenges for the next decade. *Front. Mar. Sci.* **6**, 425.

WANG, P. & ÖZGÖKMEN, T.M. 2018 Langmuir circulation with explicit surface waves from moving-mesh modeling. *Geophys. Res. Lett.* **45** (1), 216–226.

WU, J. & DEIKE, L. 2021 Wind wave growth in the viscous regime. *Phys. Rev. Fluids* **6** (9), 094801.

WU, L., RUTGERSSON, A. & SAHLÉE, E. 2015 Upper-ocean mixing due to surface gravity waves. *J. Geophys. Res.: Oceans* **120** (12), 8210–8228.

XUAN, A., DENG, B.-Q. & SHEN, L. 2019 Study of wave effect on vorticity in Langmuir turbulence using wave-phase-resolved large-eddy simulation. *J. Fluid Mech.* **875**, 173–224.

XUAN, A. & SHEN, L. 2019 A conservative scheme for simulation of free-surface turbulent and wave flows. *J. Comput. Phys.* **378**, 18–43.

YANG, D. & SHEN, L. 2011*a* Simulation of viscous flows with undulatory boundaries. Part I. Basic solver. *J. Comput. Phys.* **230** (14), 5488–5509.

YANG, D. & SHEN, L. 2011*b* Simulation of viscous flows with undulatory boundaries. Part II. Coupling with other solvers for two-fluid computations. *J. Comput. Phys.* **230** (14), 5510–5531.

ZONTA, F., ONORATO, M. & SOLDATI, A. 2016 Decay of gravity-capillary waves in air/water sheared turbulence. *Intl J. Heat Fluid Flow* **61**, 137–144.

ZONTA, F., SOLDATI, A. & ONORATO, M. 2015 Growth and spectra of gravity–capillary waves in countercurrent air/water turbulent flow. *J. Fluid Mech.* **777**, 245–259.